ARTICLE

Multi-stage metal enrichment and formation of gold mineralization in black shales: the role of high heat flow in a rift setting

Jan Pašava[1] · Lukáš Ackerman[1,2] · Jiří Žák[3] · Martin Svojtka[2] · Tomáš Magna[1] · Ondřej Pour[1] · Jakub Trubač[4] · František Veselovský[1]

Abstract

Black shales may serve as an important source of metals such as Co, Ni, or As, largely due to anoxic to euxinic conditions in association with high concentrations of sulfur leading to efficient scavenging and transport of metals from seawater into the seafloor sediment. We report on an unusual type of Au mineralization newly discovered in Ediacaran trench-slope black shales in the Bohemian Massif, Czech Republic. The Au enrichment is related to the formation of a quartz–sulfide vein system and a progressive evolution of ore-forming fluids with decreasing temperature, from Sb- to As-rich to final precipitation of native gold from silica and Au-bearing low-temperature hydrothermal colloidal solutions. The hydrothermal nature of these solutions is also documented by Li contents and isotope compositions which differ markedly between barren black shales and those carrying significant late-stage quartz-rich veins. The structural relationships and orientation of the associated quartz veins point to a close connection between vein emplacement and high heat flow in response to Ordovician rifting, and breakup of the northern margin of Gondwana, and opening of the Rheic Ocean. This triggered metal and sulfur remobilization, including Au, from the associated Neoproterozoic–Cambrian volcanosedimentary successions. The documented Au mineralization and its association with the Ordovician rift-related magmatic activity is different from the widespread Variscan Au occurrences in the Bohemian Massif. Our study thus provides a new genetic model potentially important for future exploration of Au also in other terrains underlain by a rifted Cadomian basement.

Keywords Cadomian orogeny · Gold mineralization · Black shale · Cambro–Ordovician rifting · Quartz hydrothermal veins · Polyphase deformation

Introduction

Black shales, marine siliciclastic rocks with > 1 wt% of total organic carbon (TOC) content, may serve as an important source of metal accumulations, notably redox-sensitive

✉ Lukáš Ackerman
ackerman@gli.cas.cz

1 Czech Geological Survey, Geologická 6, Praha 5 152 00, Czech Republic

2 Institute of Geology of the Czech Academy of Sciences, Rozvojová 269, Praha 165 006, Czech Republic

3 Institute of Geology and Paleontology, Faculty of Science, Charles University, Albertov 6, Praha 2 128 43, Czech Republic

4 Institute of Geochemistry, Mineralogy and Mineral Resources, Faculty of Science, Charles University, Albertov 6 128 43, Czech Republic

metals such as Mo, Ni, Cu, and U (e.g., Oszczepalski 1989; Loukola-Ruskeeniemi and Heino 1996; Coveney and Pašava 2004; Lehmann et al. 2016; Romer and Cuney 2018). This is largely due to strongly reducing conditions (anoxic to euxinic) associated with high concentration of sulfur during black shale deposition, leading to efficient scavenging and transport of metals from seawater into the seafloor sediment (e.g., Brumsack 2006; Tribovillard et al. 2012; Little et al. 2015). Additionally, elevated Au contents associated with black shales have been reported in many areas related either to syndepositional and diagenetic pyrite (e.g., Large et al. 2015; Steadman et al. 2015; Hu et al. 2016; Pašava et al. 2017; Sack et al. 2018) or quartz–sulfide veinlets and stringers (e.g., Wang et al. 2014). In this respect, several studies have highlighted the worldwide importance of black shales as a source of Au and As in sediment-hosted orogenic and Carlin-type gold deposits (Mehrabi and Yardley 1999; Large et al. 2009, 2011; Pašava et al. 2013; Selvaraja et al. 2017).

One of the prominent locations where black shales, and their metamorphic equivalents, of various ages (Ediacaran to Devonian) occur in a variety of tectonic settings is the Bohemian Massif in Central Europe (Fig. 1). The Bohemian Massif is otherwise well-known for abundant quartz–sulfide or carbonate–quartz Au deposits (Morávek and Pouba 1987; Zachariáš et al. 2013, 2014; Němec and Zachariáš 2017) hosted by late Neoproterozoic–early Cambrian volcano-sedimentary complexes of the Teplá–Barrandian Unit (~ 630–520 Ma; Sláma et al. 2008; Drost et al. 2011; Hajná et al. 2018; Žák et al. 2020) and arious units metamorphosed during the Variscan orogeny (ca. 400–300 Ma; Franke 2006; Kroner and Romer 2013; Edel et al. 2018; Schulmann et al. 2022 and references therein). About ~ 150 sites of gold mineralization have been targeted for research, exploration, and mining since medieval times (Morávek 1996). These occurrences, which are mostly of orogenic or intrusion-related gold deposit type, formed through hydrothermal activity related to magmatism/metamorphism during the Variscan orogeny and associated metal remobilization (Morávek 1996; Zachariáš et al. 2014). The Au occurrences, some of which constitute economically important Au deposits, formed between ca. 347 and 337 Ma (e.g., Mokrsko-Čelina, Kašperské Hory; Zachariáš et al. 2001, 2013; Ackerman et al. 2019). Surprisingly, despite a great number of occurrences some of which are fairly voluminous, and an assumption that volcanosedimentary successions are the most likely source of Au (Morávek and Pouba 1987), no Au occurrence has previously been reported from the black shales, except for auriferous carbonate–quartz veins in Devonian organic-rich phyllite in the northeastern part of the Bohemian Massif (Aichler et al. 1990).

In this study, we report on a new discovery of Au mineralization hosted by Ediacaran black shales in the Bohemian Massif. We first investigate field relationships, microstructures, mineralogy, and geochemistry and then examined the relative importance of silica and metal enrichment during deposition, multiple phases of superposed deformation, and subsequent hydrothermal processes. This integrated approach reveals that the Au mineralization was most likely linked to an Ordovician high heat flow event related to rifting and initial stages of breakup of the northern margin of Gondwana. Thus, our study hints at a new genetic type of Au mineralization that is different from other black shale-related Au occurrences reported so far in the European Variscan belt.

Geological setting

The Au occurrence discovered in this study (referred to as the Žloukovice section) is hosted by black shales that are part of an thick marine shale–graywacke succession of the extensive late Neoproterozoic (Ediacaran) to Early Cambrian Blovice accretionary complex (Fig. 1a, b). This complex formed during the Cadomian orogeny, as part of a long-lived subduction/accretionary system along the northern Gondwana periphery and now underlies much of the Teplá–Barrandian Unit (e.g., Hajná et al. 2013, 2018; Žák et al. 2020). The accretionary complex is composed of basalt-bearing mélanges with a block-in-matrix fabric (Belts 1–3), a chert–graywacke mélange (Belt I), and coherent, bedded units without cherts and basalts (Belts II–III; Fig. 1c).

Belt I that hosts the Žloukovice section is a SE–NW oriented, ~ 100-km long and ~ 10-km wide lithologically uniform chert–graywacke unit (Fig. 1c). The chert forms blocks up to several hundred meters in length, enclosed within siliciclastic matrix, which is dominated by fine-grained graywacke, siltstone, and shale (Ackerman et al. 2023). The chert–graywacke unit has been interpreted as an olistostrome formed presumably on a trench slope, overlain by a monotonous graywacke succession (Hajná et al. 2019). Interestingly, basalt blocks are absent and black shales are rare in Belt I unlike the other mélange belts. Elsewhere, the black shales have been interpreted as deposits of trench-slope basins during periods of limited siliciclastic supply (Kurzweil et al. 2015; Pašava et al. 2021). The published U–Pb detrital zircon geochronology constrains the age of the chert–graywacke unit to ca. 591–571 Ma (Žák et al. 2020), which is consistent with the maximum depositional age of a graywacke collected at the Žloukovice section and determined at 571 ± 3 Ma (U–Pb dating of zircon; Pašava et al. 2018).

After the Cadomian orogeny had ceased, the entire area was affected by a Cambro–Ordovician rifting phase related to the opening of the Rheic Ocean (e.g., Nance et al. 2010 and references therein), which resulted in widespread crustal extension, thinning and vigorous magmatic activity (Žák et al. 2013). To the west and southwest of the Žloukovice section, the extensive subaerial andesitic–rhyolitic Křivoklát–Rokycany volcanic complex (KRVC; Fig. 1) erupted during the late Cambrian (ca. 500–485 Ma; Drost et al. 2004; Žák et al. 2013; Kolářová et al. 2022). During the early Ordovician, the chert–graywacke unit was transgressively overlain by the rift-related Prague Basin fill, with deposition accompanied by extensive predominantly submarine basaltic volcanism forming the Komárov Volcanic Complex to the southeast of the Žloukovice section (Fig. 1d; Patočka et al. 1993; Chlupáč et al. 1998).

Field and structural relationships

The Žloukovice section represents a ~ 150-m long, continuous, NW–SE-oriented natural outcrop (50.01026N, 13.95889E; Fig. 2a) located on the right bank of the Berounka River, about 35 km west of Prague (Fig. 1c). The

section exposes a uniformly dipping package representing the siliciclastic matrix of the chert–graywacke unit (Belt I) where several layers of black shales are intercalated with a monotonous succession of shale, siltstone, and fine-grained graywacke. The latter is mostly dark gray to grayish in color due to variable but still significant amounts of organic matter (Fig. 2a). The whole package was pervasively overprinted by late Cadomian deformation, resulting in pressure-solution cleavage, under low-temperature, anchimetamorphic to lower greenschist-facies conditions. Consequently, the primary depositional features and bedding are not discernible, except for the black shale-graywacke contacts (Fig. 2a). The cleavage dips to the ~NNW to NNE at 20–40°.

Macroscopic quartz veins occur in several clusters along the section: they are rather rare in the monotonous succession but are abundant within the main black shale layer (Fig. 2a). The veins are typically several millimetres to 1–2-cm thick with an average spacing of about 10–30 cm (Fig. 2b). Thicker veins exhibit elongate blocky quartz crystals oriented perpendicular to the vein plane (Fig. 2b). The veins dip steeply, cutting across the cleavage at a high angle (Fig. 2b), and strike predominantly ~ENE–WSW (Fig. 2c). In addition, the lower part of the main black shale layer is cross-cut by two prominent sets of extension fractures (joints), one striking ~ N–S to ~ NNE–SSW, and the other ~ E–W (Fig. 2c). These joints are mostly barren, but in places are filled with quartz.

Samples and methods

In total, 18 representative samples were taken along the Žloukovice section. Nine samples were collected over a distance of ca. 100 m from the monotonous succession in the southeastern part of the section, for the sake of simplicity we refer to these rocks as "normal" black shales (hereafter abbreviated as NBS; samples 17CB09/1 to 17CB09/3 and 17CB09/5 to 17CB09/09; Fig. 2a) which are devoid of quartz veinlet clusters. Other nine samples are NBS that contain abundant, but variable amounts of quartz vein clusters (hereafter abbreviated as SIBS; sample 17CB09/4 and 17CB09/10 to 17CB09/17; the latter sample was also used for U–Pb dating; Fig. 2a). Finally, one sample of NBS was collected once again in the northwestern part of the section (17CB09/18; Fig. 2a).
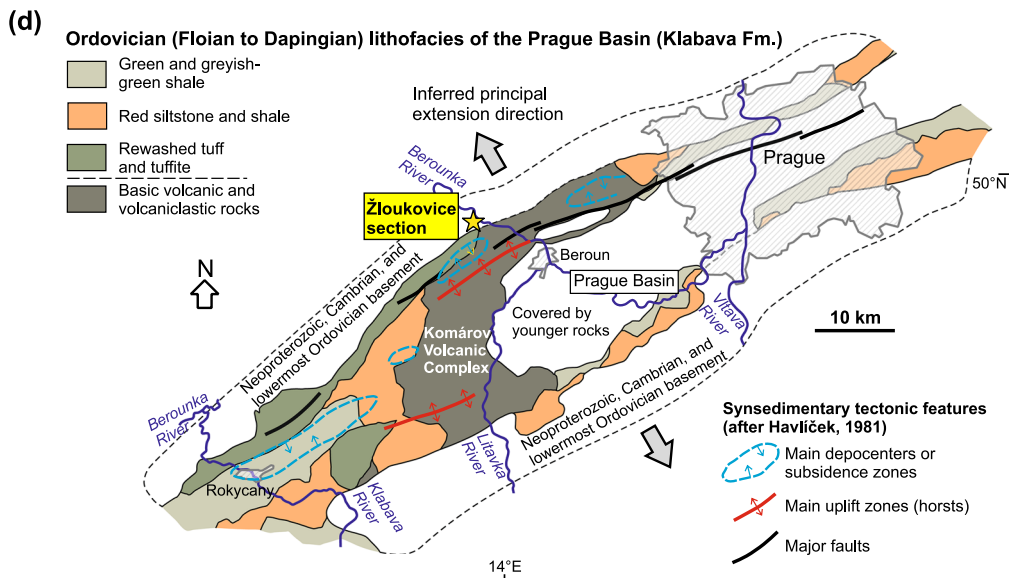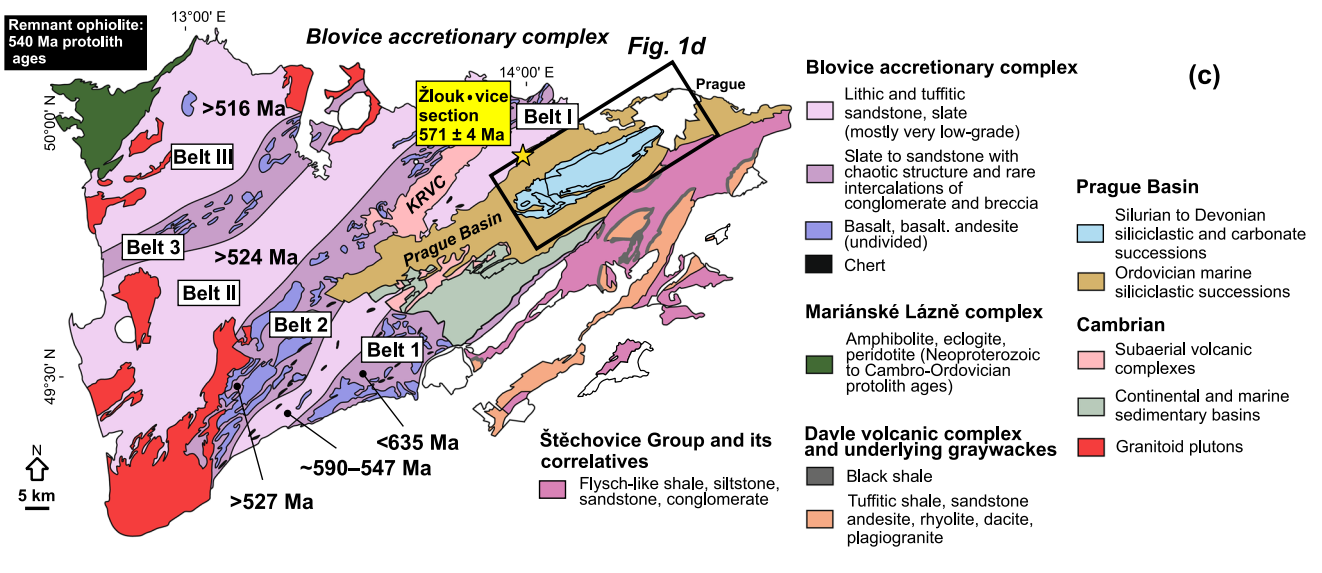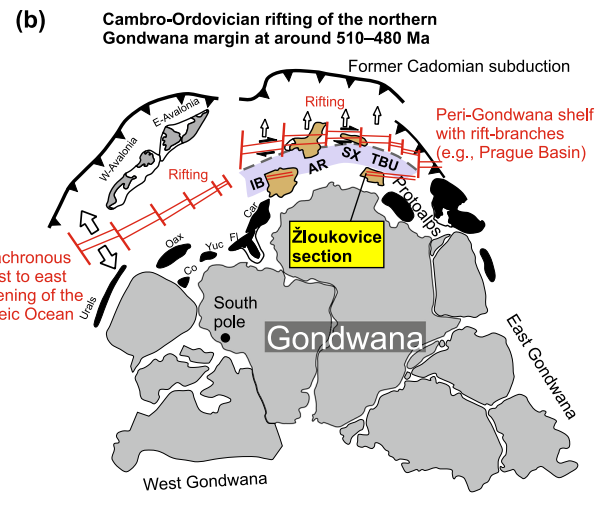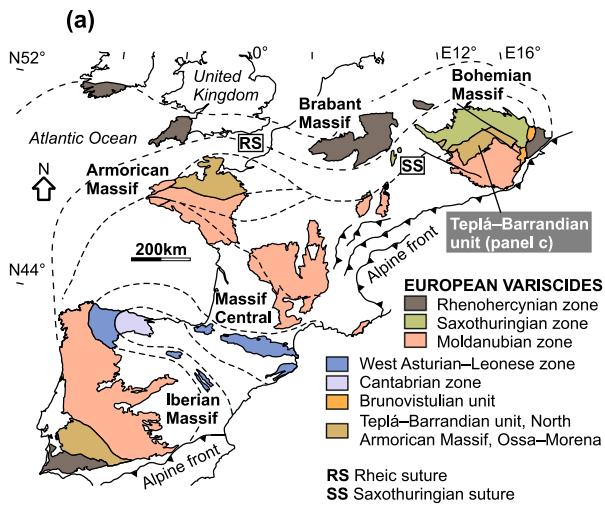
The polished thin sections were first examined using a conventional reflected light microscope and a Tescan *Mira3 GMU* FE–SEM scanning microscope, housed at the Czech Geological Survey, Prague. Subsequently, representative pyrite and pyritized marcasite grains were selected for in situ trace element analysis using an *Element 2* ICP-MS (ThermoFisher Scientific, Bremen, Germany) coupled with a 193-nm Analyte (Excite) excimer laser ablation system (Teledyne Cetac, Omaha, USA), housed at the Institute of

Geology of the Czech Academy of Sciences, Prague. Samples were fired at a repetition rate of 10 Hz, the laser fluency was 3 J.cm^{-2}, and the laser beam spot size was 16–50 µm according to the size of grains. The analyzed elements were calibrated against the synthetic sulfide reference material MASS-1 (USGS) with ^{57}Fe mass used as internal standard. The time-resolved signal data were processed using the Glitter software (van Achterbergh et al. 2001). The precision of the laser ablation analyses ranged between 5 and 15% (1RSD) for most elements. The accuracy of the protocol was monitored by the synthetic glass reference material STDGL3 with the results being in good agreement with those reported previously (Belousov et al. 2016).

Major element concentrations were determined using conventional wet chemistry methods (see Dempírová et al. 2010) at the Czech Geological Survey, Prague, with the internal precision better than 5% (RSD), whereas the long-term reproducibility of selected reference materials (e.g., JG-3) was better than 10% for all the analyzed element oxides. Trace element contents were acquired using an *iCAP-Q* ICP-MS (ThermoFisher Scientific, Bremen, Germany), housed at the Faculty of Science, Charles University, following the methods detailed in Strnad et al. (2005). The in-run precision was always better than 5%, and the accuracy was better than 12% for all analyzed elements, based on the analyses of SBC-1 and SGR-1b reference materials (shale and petroleum-rich shale, respectively; USGS).

Analyses of Au concentrations were carried out using an Agilent 7900 ICP-MS following the leaching of samples using NaCl saturated in Br, performed at the Czech Geological Survey, Prague. The precision of the analyses was better than 5%, whereas the long-term reproducibility of the analyses was monitored using selected reference materials (CH4 gold ore, CANMET) with the results better than ± 10% with respect to recommended values. This method has a detection limit of 4 ppb for Au.

Lithium abundance and isotopic composition in bulk-rock samples, separated quartz, and quartz-free matrix were acquired at the Czech Geological Survey, Prague, using the established analytical and instrumental protocols (Magna et al. 2004, 2006). A Neptune MC-ICP-MS (ThermoFisher Scientific, Bremen, Germany) was employed to determine the Li contents and isotope ratios. For seven selected samples (two NBS, five SIBS), quartz and quartz-free matrix were also analyzed in addition to bulk-rock samples to test any possible differences in Li content and isotopic composition for these two shale types, distinguished by their respective post-depositional histories. The final data are reported relative to the L-SVEC reference material (Flesch et al. 1973) and reported as $\delta^7\mathrm{Li}$ (‰) $= [(^7\mathrm{Li}/^6\mathrm{Li})_{\mathrm{sample}}/ (^7\mathrm{Li}/^6\mathrm{Li})_{\mathrm{L\text{-}SVEC}} - 1] \times 1000$. The entire analytical and instrumental procedure was monitored using the international reference materials and analyzed along with the unknown samples. Their $\delta^7\mathrm{Li}$ values are listed in Table 1 and are consistent with the reported values (Jochum et al. 2005).

(a) European Variscides overview map showing Bohemian Massif, Brabant Massif, Armorican Massif, Massif Central, Iberian Massif, Teplá–Barrandian unit (panel c).

EUROPEAN VARISCIDES
- Rhenohercynian zone
- Saxothuringian zone
- Moldanubian zone
- West Asturian–Leonese zone
- Cantabrian zone
- Brunovistulian unit
- Teplá–Barrandian unit, North Armorican Massif, Ossa–Morena

RS Rheic suture
SS Saxothuringian suture

(b) Cambro-Ordovician rifting of the northern Gondwana margin at around 510–480 Ma

Former Cadomian subduction. Rifting. Peri-Gondwana shelf with rift-branches (e.g., Prague Basin). Žloukovice section. Diachronous west to east opening of the Rheic Ocean. South pole. Gondwana. West Gondwana. East Gondwana.

(c) *Blovice accretionary complex* Fig. 1d

Remnant ophiolite: 540 Ma protolith ages

>516 Ma, Belt III, Belt 3, >524 Ma, Belt II, Belt 2, Belt 1, <635 Ma, ~590–547 Ma, >527 Ma

Žloukovice section 571 ± 4 Ma, Belt I, KRVC, Prague Basin, Prague

Blovice accretionary complex
- Lithic and tuffitic sandstone, slate (mostly very low-grade)
- Slate to sandstone with chaotic structure and rare intercalations of conglomerate and breccia
- Basalt, basalt. andesite (undivided)
- Chert

Mariánské Lázně complex
- Amphibolite, eclogite, peridotite (Neoproterozoic to Cambro-Ordovician protolith ages)

Davle volcanic complex and underlying graywackes
- Black shale
- Tuffitic shale, sandstone andesite, rhyolite, dacite, plagiogranite

Štěchovice Group and its correlatives
- Flysch-like shale, siltstone, sandstone, conglomerate

Prague Basin
- Silurian to Devonian siliciclastic and carbonate successions
- Ordovician marine siliciclastic successions

Cambrian
- Subaerial volcanic complexes
- Continental and marine sedimentary basins
- Granitoid plutons

(d) Ordovician (Floian to Dapingian) lithofacies of the Prague Basin (Klabava Fm.)
- Green and greyish-green shale
- Red siltstone and shale
- Rewashed tuff and tuffite
- Basic volcanic and volcaniclastic rocks

Inferred principal extension direction. Berounka River. Žloukovice section. Prague. Beroun. Prague Basin. Covered by younger rocks. Neoproterozoic, Cambrian, and lowermost Ordovician basement. Komárov Volcanic Complex. Vltava River. Litavka River. Klabava River. Rokycany. Berounka River.

Synsedimentary tectonic features (after Havlíček, 1981)
- Main depocenters or subsidence zones
- Main uplift zones (horsts)
- Major faults

10 km

◀**Fig. 1** **a** Map of the Variscan orogenic belt in western and central Europe showing position of the Bohemian Massif and Teplá–Barrandian Unit. **b** Palinspastic reconstruction of the northern margin of Gondwana during Cambro–Ordovician rifting related to opening of the Rheic Ocean (modified from Linnemann et al. 2004 and Hajná et al. 2018). **c** Geologic map of the Teplá–Barrandian Unit showing location of the Žloukovice section within the olistostromal Belt I. Age ranges refer to the maximum depositional ages of the siliciclastic successions inferred from the U–Pb zircon geochronology (Žák et al. 2020). *KRVC* Křivoklát–Rokycany volcanic complex. **d** Map of facies distribution and syn-sedimentary faults in the Prague Basin during the Early to Middle Ordovician, indicating ~ NW–SE crustal extension. Note the position of the Žloukovice section at the margin of a large volcanic center (modified from Žák et al. 2013)

Pyrite separates were prepared by a combination of crushing, hand picking, and leaching, resulting in > 95% purity of the separates. Sulfur isotopic compositions of pyrite as well as those of bulk rocks were determined at the Laboratory for Stable and Radiogenic Isotopes at the Faculty of Science, Charles University, using methods detailed in Pašava et al. (2021).

Results

Microstructures

Whereas the macroscopic quartz veins appear undeformed, exhibit quite a uniform orientation, and cut across the regional cleavage at a high angle (Fig. 2), more complex relationships and several generations of quartz veins were noticed in the SIBS on a microscale (Fig. 3). We distinguish these different vein generations mainly based on their geometry and structural (and inferred temporal) relationships to the host deformational microstructures:

(1) The oldest veins were folded into close to isoclinal microfolds (Qtz I), with their limbs commonly exhibiting pinch-and-swell structures or boudinage and axial planes parallel to the continuous cleavage (Fig. 3a), corresponding to the lower greenschist-facies conditions in this part of the Blovice accretionary complex (Hajná et al. 2010). The vein interiors are also, in places, dynamically recrystallized into a mosaic of smaller grains surrounding larger quartz grains and aggregates.

(2) Younger veins (Qtz II) cut at an angle the previous generation and are subparallel to localized contractional kink bands that overprint the cleavage (Fig. 3a). They appear to utilize, at least partly, the kink planes and exhibit a pinch-and-swell structure or are even boudinaged (Fig. 3a). This generation of veins thus post-dates the regional deformation but is coeval with the development of contractional kink bands, interpreted as a result of pre-Variscan (late Cadomian) deformation by Hajná et al. (2010).

(3) The youngest observed veins (Qtz III) cut across both cleavage and kink bands at a high angle and are straight, with various lengths from about 1 mm (Fig. 3b) to at least
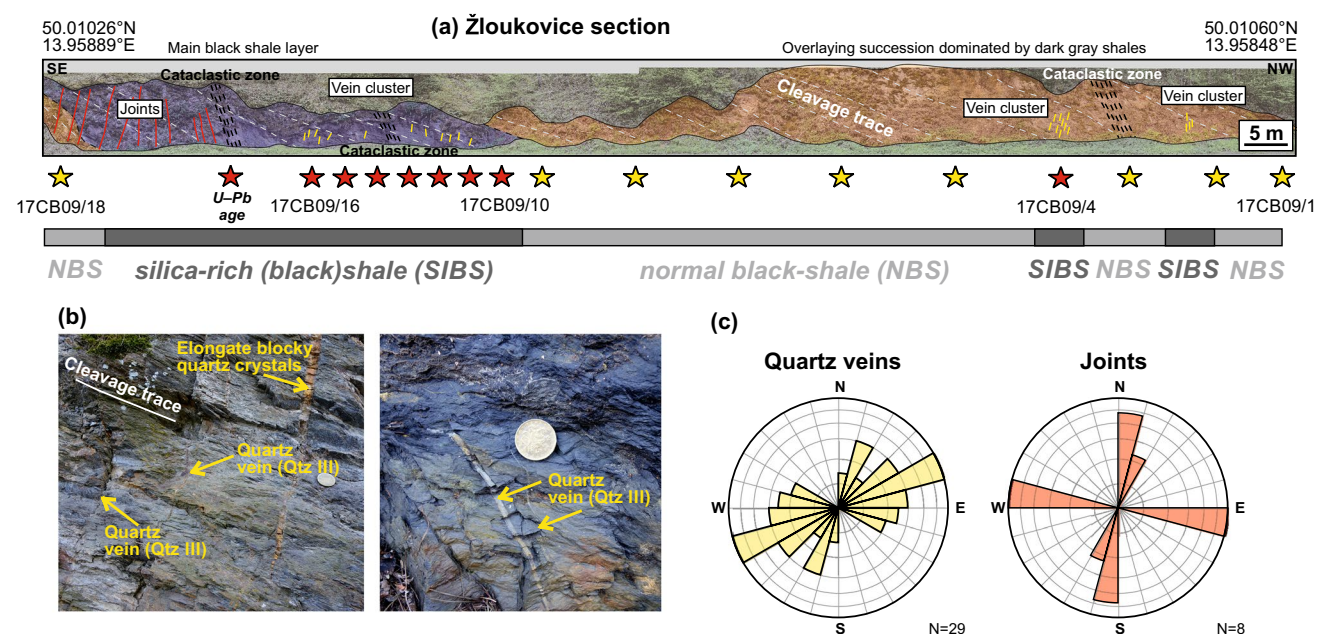
Fig. 2 **a** Photomosaic of the Žloukovice section showing lithologic units, i.e., the main black shale layer (silicified black shales, SIBS) and overlaying succession dominated by dark gray shales (normal black shales, NBS) and the principal vein clusters. **b** Close-up views on the discordant Qtz III veins within the main black shale layer that cut across the Cadomian regional cleavage. **c** Rose diagrams summarizing orientation of the Qtz III veins and joints along the section. The yellow and red stars mark the position of the collected NBS and SIBS samples, respectively

Table 1 Lithium elemental and isotopic compositions of the bulk rocks, quartz veins, and quartz-free matrix and sulfur isotopic composition of pyrites from the studied normal and silica-rich black shales (NBS and SIBS, respectively)

Sample	Lithology	Li (ppm)	δ^7Li (‰)	2SD	δ^{34}S (‰) pyrite	2SD
17CB09/01	NBS	31.6	−0.40	0.33	−18.1	2.2
17CB09/02	NBS	40.1	1.62	0.16	−12.6	1.1
17CB09/03	NBS	37.4	0.31	0.19	−13.5	0.3
	Qtz-vein (Qtz III)	138	18.58	0.10		
	Qtz-free matrix	36.4	0.63	0.10		
17CB09/04	SIBS	49.0	6.11	0.26	−12.6	0.3
	Qtz-vein (Qtz III)	227	18.94	0.24		
	Qtz-free matrix	41.3	3.11	0.13		
17CB09/05	NBS	48.6	−0.61	0.34	−13.5	1.0
17CB09/06	NBS	60.0	−1.74	0.31	−10.8	0.4
17CB09/07	NBS	38.0	−1.02	0.14	−15.8	0.6
17CB09/08	NBS	42.2	0.03	0.23	−18.8	1.1
17CB09/09	NBS	52.5	−0.98	0.05	−20.5	0.6
17CB09/10	SIBS	58.2	2.30	0.15	−18.8	0.1
	Qtz-vein (Qtz III)	281	17.98	0.09		
	Qtz-free matrix	60.5	10.13	0.14		
17CB09/11	SIBS	66.8	14.80	0.22	−20.6	0.5
17CB09/12	SIBS	57.9	11.98	0.24	−17.6	0.4
17CB09/13	SIBS	54.3	12.46	0.30	−18.1	0.1
	Qtz-vein (Qtz III)	44.9	18.45	0.23		
	Qtz-free matrix	35.4	8.05	0.16		
17CB09/14	SIBS	96.0	15.66	0.28	−19.2	0.4
	Qtz-vein ± carbonate	123	17.44	0.10		
	Qtz-free matrix	97.7	16.35	0.13		
17CB09/15	SIBS	63.1	12.73	0.07	−19.4	0.1
	Qtz-vein (Qtz III)	100	17.25	0.13		
	Qtz-free matrix	34.5	11.60	0.08		
17CB09/16	SIBS	44.3	15.50	0.09	−18.1	0.7
17CB09/17	SIBS	79.1	16.04	0.23	−19.6	0.4
	Qtz-vein (Qtz III) ± carbonate	273	18.43	0.20		
	Qtz-free matrix	251	15.50	0.25		
17CB09/18	NBS	25.3	−0.51	0.26	−18.8	0.1
Reference materials						
BHVO-2	Basalt	4.90	4.58	0.11		
duplicate		4.62	4.59	0.17		
JG-2	Granite	40.1	0.12	0.11		
JR-2	Rhyolite	81.0	3.89	0.07		
JSd-3	Stream sediment	163	−1.47	0.08		
G-3	Granite	32.8	0.75	0.16		
SGR-1b	Shale	147	3.99	0.23		

several centimeters (Fig. 3c, d). In some cases, two adjacent veins define narrow domains in which the cleavage is abruptly deflected and rotated or form elongated parallelogram-shaped segments (Fig. 3c), both indicating non-coaxial vein opening. These Qtz III veins correspond to those observed macroscopically on the outcrop (Fig. 2b).

In fine-grained graywacke, structural relationships are simpler as the quartz veins are much rarer and kink bands are not frequently developed, but it is still possible to recognize

both the early and late generation, the former boudinaged and recrystallized and the latter cutting across the continuous cleavage.

Petrography and mineral chemistry

The principle syndepositional/early diagenetic sulfide phase that occurs in NBS as well as SIBS rock matrix is slightly recrystallized pyrite (Py I), forming framboidal or irregular
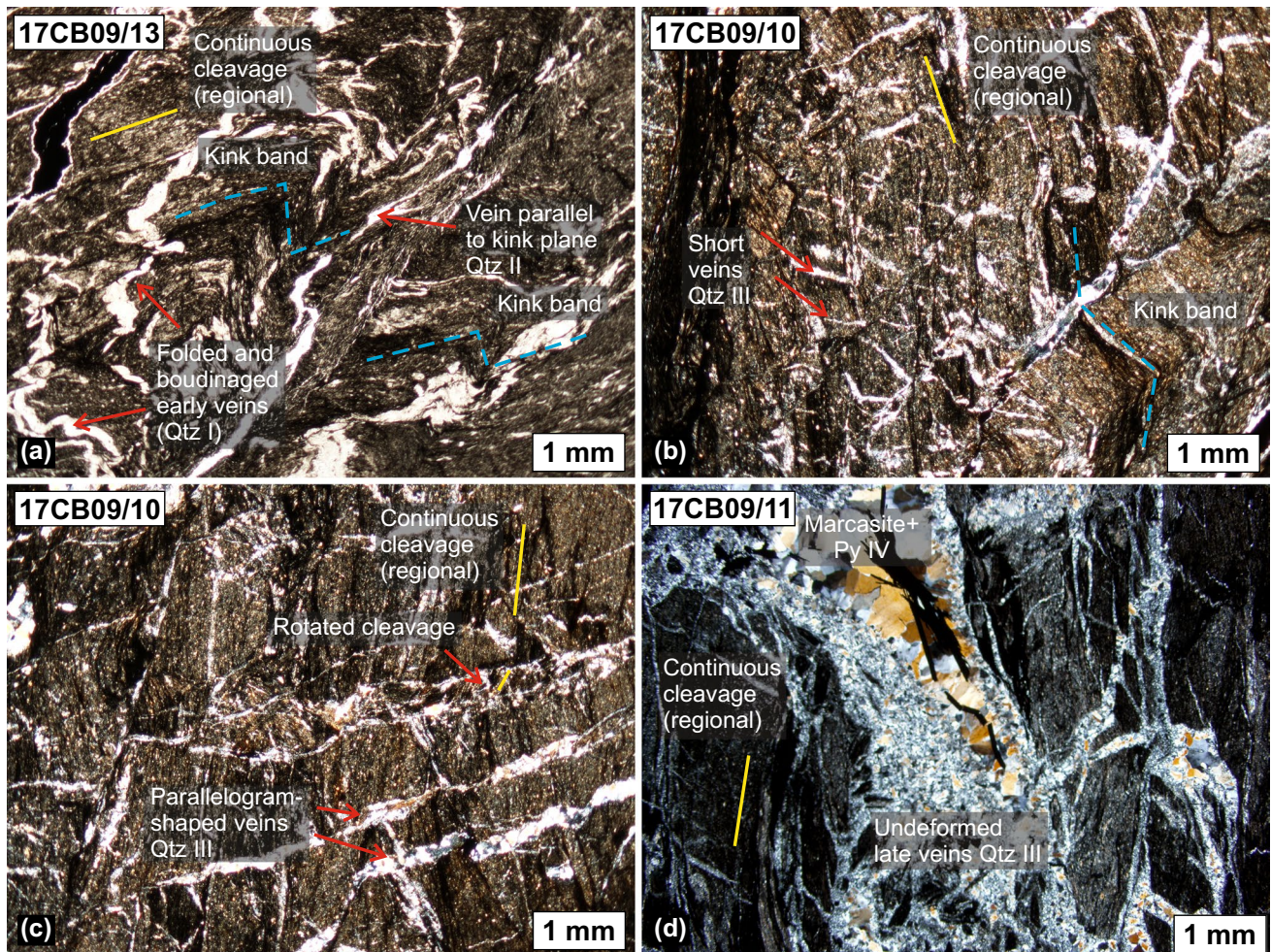
Fig. 3 **a–d** Photomicrographs (under crossed polars) to show the different generations of veinlets in black shales (see text for description)

grains, cubes (mostly < 10 μm), aggregates (Fig. 4a), and layers. This type of pyrite has high contents of metals such as As, Ag, Au, Bi, Co, Hg, Ni, Pb, Zn, and Sb (Table 2) whereas its low Ni/Co (< 2.1) ratio confirms its sedimentary origin. Its Au contents (mean ~ 0.6 ppm) are positively correlated with Ag, Pb, Hg, and Sb without any relationship to the As abundance. The transformation of Py I aggregates resulted in the formation of diagenetic pyrite nodules (Py II; Fig. 4b). Some samples that are particularly rich in sulfur (e.g., 17CB09/11 with 0.69 wt% S) contain strongly deformed layers that consist of large and commonly euhedral and zonal pyrite grains (Py III; Fig. 4c) formed through the transformation of Py I. Overall, the transformation (Py I → Py II → Py III) was accompanied by a progressive decrease in Co, Ni, Zn, Mn, and Ag contents and an increase in the Ni/Co ratio (Table 2).

The late-stage undeformed quartz veins host abundant *marcasite* that is notably enriched in Sb and Hg (up to ~ 12,000 and 534 ppm, respectively), whereas Au and Se contents are low (Fig. 5, Table 2). Marcasite is either associated with another generation of pyrite (Py IV; Fig. 4e) that also forms individual veinlets with generally low trace element contents (Table 2) or, more commonly, forms characteristic "spicule"-like grains associated with fracturing and selective dissolution of grains and their replacement by *pyritized marcasite* (Fig. 4f). The LA-ICP-MS analyses and mapping revealed that pyritization was largely connected with enrichment in Au (up to 11 ppm), As (up to ~ 3200 ppm), and Se (207 ppm; Table 2). Nickel and Se are predominantly concentrated in the marcasite rims whereas Au is irregularly distributed within the grains (Fig. 5). This stage is further documented by the latest pyrite generation (Py V) developed on the rims of Py III that underwent apparent dissolution and resorption (Fig. 4d). Similarly to pyritized marcasite, the Py V is largely enriched in As, Se, and Au (e.g., As up to 3 wt%, Au up to 19 ppm; Table 2; Fig. 5). Collectively, very low Au/As ratios (< 0.004) of all pyrite generations suggest that Au is present in the form of solid solution (Reich et al. 2005; Deditius et al. 2014).
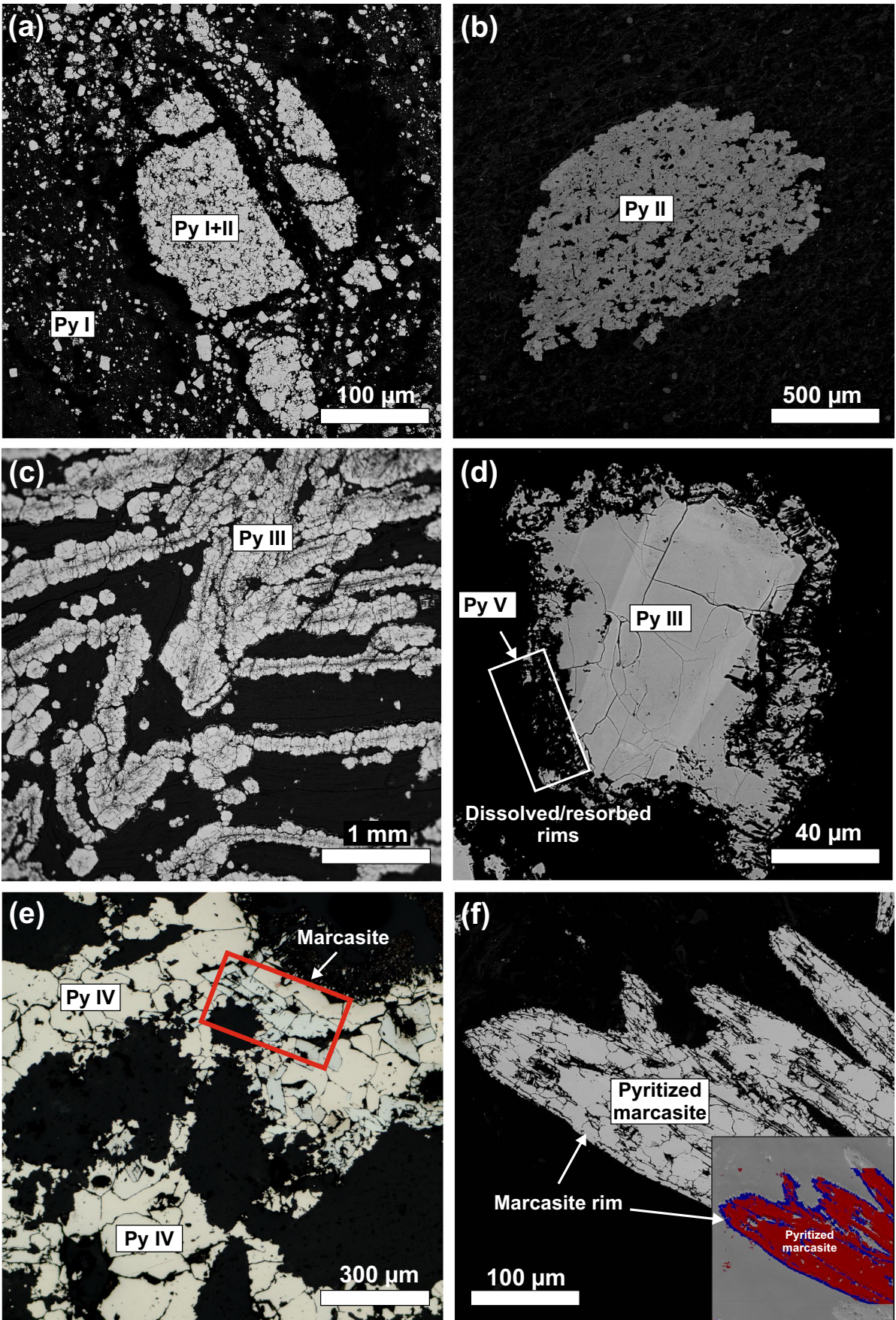
Fig. 4 a–e Petrography and textures of five pyrite generations (Py I–V) together with marcasite and pyritized marcasite (see text for details)

Native gold is present in the form of rare dendritic aggregates within up to 500-μm long "branches" of different orientation being present only in the matrix of silica-rich shales whereas either marcasite–pyrite or pyrite veinlets are found nearby (Fig. 6a, b). Gold forms skeletal crystals associated with Si-rich material devoid of any sulfides (Fig. 6c, d). Overall, these aggregates are characterized by the presence of pores within the Si-rich domains and by largely variable Au–Si–O proportions (Fig. 6c, d).

Major and trace element concentrations and metal enrichments

The analyses of major and trace elements corroborate the presence of two different types of shale in the studied section: (1) normal black shale (NBS; sensu Pašava 2000) and (2) silica–As–Sb-rich black shale (SIBS), in places with elevated Au contents. In comparison to the SIBS, the NBS is characterized by lower contents of SiO_2 (60.1–63.0 wt%; Fig. 7a) and S (≤ 0.18 wt%; Fig. 7d) whereas it is enriched in all other major elements (see Na_2O versus SiO_2 as an example of typical patterns; Fig. 7c). Only the K_2O and Fe_2O_3 contents overlap for both groups whereas the FeO contents are significantly higher for the NBS samples (Fig. 7b; Supplementary Table 1). The NBS sample 17CB09/18, deposited after the SIBS, has lower contents of SiO_2 and MgO but elevated K_2O and reversed FeO–Fe_2O_3 systematics compared to the other NBS samples; its slightly higher CaO content appears to be associated with minor carbonate due to elevated CO_2. The NBS samples have distinctively high contents of transitional metals (Co, Ni, Cu, Zn) and marginally higher contents of high-field strength elements (HFSE; Zr, Hf, Nb, Ta) and Th (Fig. 8). The chondrite-normalized rare earth element (REE) patterns for NBS samples show similar LREE-enrichment over HREE (Fig. 9a) with markedly negative Eu anomalies (Eu/Eu* = 0.65–0.71). When normalized to PAAS (post-Archean Australian Shale), the NBS samples exhibit convex-upward patterns characterized by MREE enrichment over LREE/HREE (Fig. 9b; La_N/Sm_N of ~ 0.8).

The Al-normalized enrichment factors (EF-X = [(X/Al)$_{sample}$/(X/Al)$_{graywacke}$], where X and Al represent the concentration of a given element and Al, respectively, have been calculated using a local graywacke sample 17CB11 (50.02663N 13.92688E; Supplementary Table 1), collected about 2 km to the NW of the Žloukovice section, as reference. The local sedimentary background was thus used for normalization which appear to be more robust than using "average shale" like PAAS (Böning et al. 2012; Little et al. 2015). In doing so, an EF > 1 indicates authigenic enrichment of the given metal, while EF < 1 indicates depletion. The calculated EFs for the NBS (Supplementary Table 1) show no systematis enrichment compared to local graywacke with the exception of higher As–Sb EF and elevated Mo–Ni–Cr EF obtained for the samples 17CB09/7 and 17CB09/18, respectively.

The SIBS exhibit a wide range of SiO_2 contents (67.6–88.3 wt%) that negatively correlate with other major elements (Fig. 7) reflecting a variable presence of quartz veinlets. In contrast to NBS and lithogenic background graywacke, the SIBS samples exhibit a marked enrichment in sulfur of up to 0.76 wt% (Fig. 7b) as well as As and Sb (e.g., EF-As and EF-Sb up to ~ 50 and ~ 114, respectively; except for sample 17CB09/4; online supplementary Table 1). Among the SIBS samples, the most SiO_2-rich sample 17CB09/16 (88.3 wt%) is exceptional in having a remarkably high TOC content of 3.3 wt% (cf. < 1 wt% found in all other studied samples), paralleled by high contents of redox-sensitive metals (e.g., V, Ni, Mo, U) and Au (~ 49 ppb; online supplementary Table 1). At the same time, it also shows significant depletion in Na_2O, Zn, Ga, and HFSE. The chondrite-normalized REE patterns of SIBS samples are similar to those of the NBS samples with subtle differences in the HREE range displaying flat to slightly HREE-elevated profiles (Fig. 9a), although the absolute REE abundances of the SIBS group are slightly lower. Consequently, the PAAS-normalized patterns also display a minor depletion of MREE relative to HREE (Fig. 9b).

Lithium concentrations and isotopic composition

The Li concentrations and isotopic compositions of the bulk rocks, separated quartz veins (Qtz III), and quartz-free matrix are listed in Table 1 and plotted in Fig. 10. Bulk-rock Li contents in the NBS samples range from 25.3 to 60.0 ppm (mean [Li] = 42.5 ± 20.6 ppm); two quartz veins have elevated Li contents of 138 and 227 ppm whereas the quartz-free matrix has Li contents similar to the bulk-rock samples. The δ^7Li ratios range from -1.74 to $+1.62‰$ in the bulk-rock samples and two quartz-free matrix samples show δ^7Li values broadly similar to their bulk-rock aliquots. Quartz from these samples displays uniformly high δ^7Li of ~ $+18.7‰$.

Bulk-rock Li contents in the SIBS samples vary between 44.3 and 96.0 ppm (mean [Li] = 65.0 ± 32.1 ppm). The quartz veins (Qtz III) are enriched in Li in four out of five samples, with Li contents of up to 281 ppm, and Li contents are also higher in three out of five quartz-free matrix aliquots compared to the corresponding bulk-rock samples. The δ^7Li in bulk-rock samples are systematically higher (from $+12.0$

Table 2 LA-ICP-MS trace element compositions (ppm) of pyrite and marcasite from the studied black shales

Phase/type		V	Cr	Mn	Co	Ni	Cu	Zn	As	Se	Ag	Sn	Sb	Au	Hg	Pb	Ni/Co	Ag/Au
Syndepositional/slightly recrystallized Pyrite I (n=5)	Mean	14	19	6.0	557	647	91	98	243	18	5.0	2.1	279	0.55	11	361	1.3	6.4
	SD	7.0	7.1	bdl	462	378	67	11	193	4.1	1.3	0.25	164	0.20	6.4	182	0.52	2.7
	Min	6.9	12	6.0	257	256	14	83	65	14	2.7	1.9	41	0.20	4.0	110	0.86	1.5
	Max	21	26	6.1	1471	1270	205	109	616	24	6.1	2.4	488	0.78	21	578	2.1	8.7
Nodular Pyrite II (n=25)	Mean	26	19	160	61	110	69	23	122	21	1.5	0.45	89	0.17	1.1	179	2.0	23
	SD	44	23	116	77	190	58	18	121	11	0.80	0.72	60	0.14	0.59	156	1.1	36
	Min	0.21	0.44	11	1.9	5.0	6.0	2.1	3.2	0.5	0.16	0.12	2.9	0.002	0.10	6.9	0.76	1.9
	Max	203	115	499	303	915	294	84	595	39	3.3	3.6	279	0.62	2.3	790	5.4	169
Pyrite III aggregates (n=23)	Mean	8.6	9.1	na	37	164	61	bdl	237	17	1.1	1.0	254	0.17	8.7	189	31	25
	SD	4.0	4.0		49	192	25		513	9.0	0.75	0.63	92	0.11	3.9	209	47	24
	Min	2.1	1.4		0.69	11	16		3.4	2.0	0.15	0.13	70	0.045	1.8	25	0.66	2.7
	Max	17.6	18		159	590	98		2225	35	2.9	2.5	487	0.4	18	791	184	92
Pyrite IV (n=24)	Mean	bdl	bdl	bdl	3.0	125	24	3.9	279	17	0.52	0.24	37	0.19	7.4	7.7	54	19
	SD				1.2	59	37	13	222	16	0.17	0.00	59	0.17	13	15	158	13
	Min				1.2	3.3	0.39	0.22	24	2.8	0.27	0.24	0.05	0.010	0.20	0.028	11	0.54
	Max				4.5	217	133	53	855	53	0.76	0.24	238	0.56	48	45	724	30
Pyrite V (n=34)	Mean	3.3	2.7	na	45	284	60	bdl	5986	50	1.0	0.35	159	2.2	4.0	213	23	8.6
	SD	3.4	1.6		30	170	21		5925	49	0.60	0.28	69	4.8	2.7	221	20	9.6
	Min	0.10	0.87		0.23	91	26		381	14	0.39	0.10	35	0.031	0.52	2.7	1.2	0.052
	Max	18.7	6.9		113	664	107		29,735	259	3.6	1.2	290	19	11	740	47	39
Marcasite (n=20)	Mean	na	na	na	2.5	8.0	25	bdl	419	6.6	2.9	na	4092	0.023	203	18	3.2	115
	SD				2.0	10	23		284	2.8	5.7		3340	0.015	161	19	2.0	258
	Min				0.05	0.50	2.8		20	2.7	0.03		52	0.010	6.3	1.0	0.31	2.5
	Max				9.4	49	104		992	13	24.6		11,914	0.055	534	91	10	1170
Pyritized marcasite (n=14)	Mean	bdl	bdl	bdl	bdl	30	26	bdl	1496	52	1.9	bdl	119	5.0	0.54	39	34	0.37
	SD					8.4	15		851	56	1.8		68	2.9	0.34	26	29	0.16
	Min					22	5.9		82	17	0.36		61	0.86	0.10	8.3	23	0.12
	Max					38	54		3176	207	6.8		326	11	1.2	103	128	0.64

na not analyzed, *bdl* below detection limit
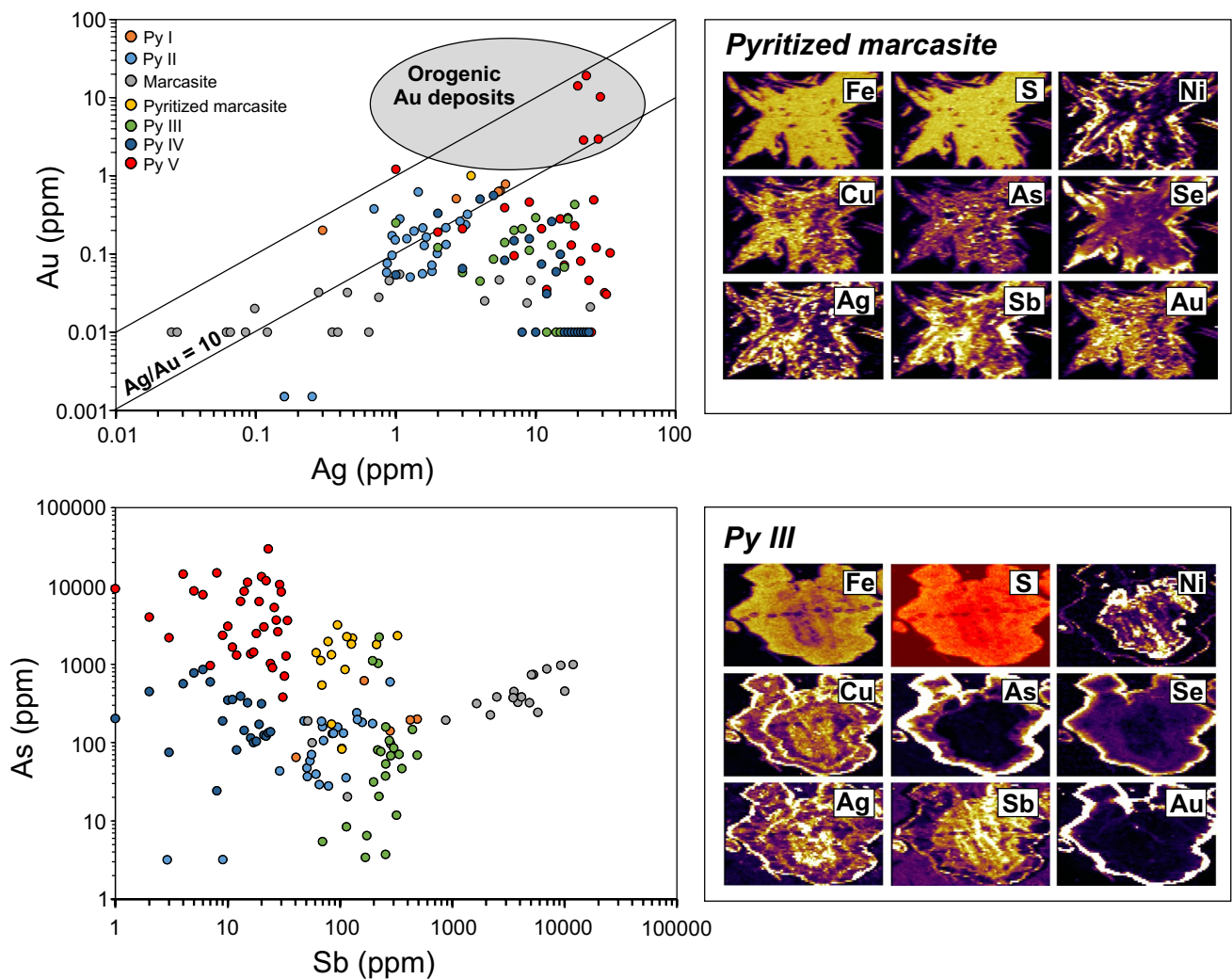
Fig. 5 Gold, Ag, Sb, and As concentrations (ppm) in the studied pyrite (Py I–V), marcasite, and pyritized marcasite determined in situ by LA-ICP-MS analyses along with elemental maps for Py III and pyritized marcasite. Note that formation of Py III and pyritization of marcasite was accompanied by a marked input of Au and As (see the text for more details)

to +16.0‰) in seven samples; the only exception is the SIBS sample 17CB09/10 with $\delta^7Li = +2.3‰$, i.e., in the range of the NBS samples. Note that this sample comes from the transition zone from the NBS to SIBS facies. All five quartz vein samples (Qtz III) from the SIBS section have elevated δ^7Li values (+17.2 to +18.5‰), well above those of the bulk-rock samples. Quartz-free matrix samples yielded slightly lower δ^7Li values in three out of five samples; Li isotope composition of the matrix in sample 17CB09/10 is significantly heavier by ~7.8‰.

Lithium contents in the NBS and SIBS samples correlate with SiO_2 contents (Fig. 10a) and fall into two discrete groups when plotted against FeO^T, with samples 17CB09/4 and 17CB09/10 (both SIBS) transitional between the two groups (not shown). Increased Li contents in the SIBS group samples also broadly correlate with Sb contents (Fig. 10b). Lithium contents negatively correlate with the

individual REE values (not shown). Lithium isotopic compositions display a strong positive covariation with SiO_2 contents and a mirror-like negative covariation with Al_2O_3 and Th (not shown). Samples 17CB09/4 and 17CB09/10 (SIBS) appear to be transitional between the two groups (Fig. 10c). In Fig. 10d, the δ^7Li values are plotted against Li content and it is apparent that the Li-rich quartz is the major carrier of isotopically heavy Li.

Sulfur isotopic composition

The sulfur isotopic compositions of separated pyrite grains are summarized in Table 1. The $\delta^{34}S_{V-CDT}$ values for the whole sample set range from −20.6 to −10.8‰ with no direct relationship between the NBS and SIBS groups,
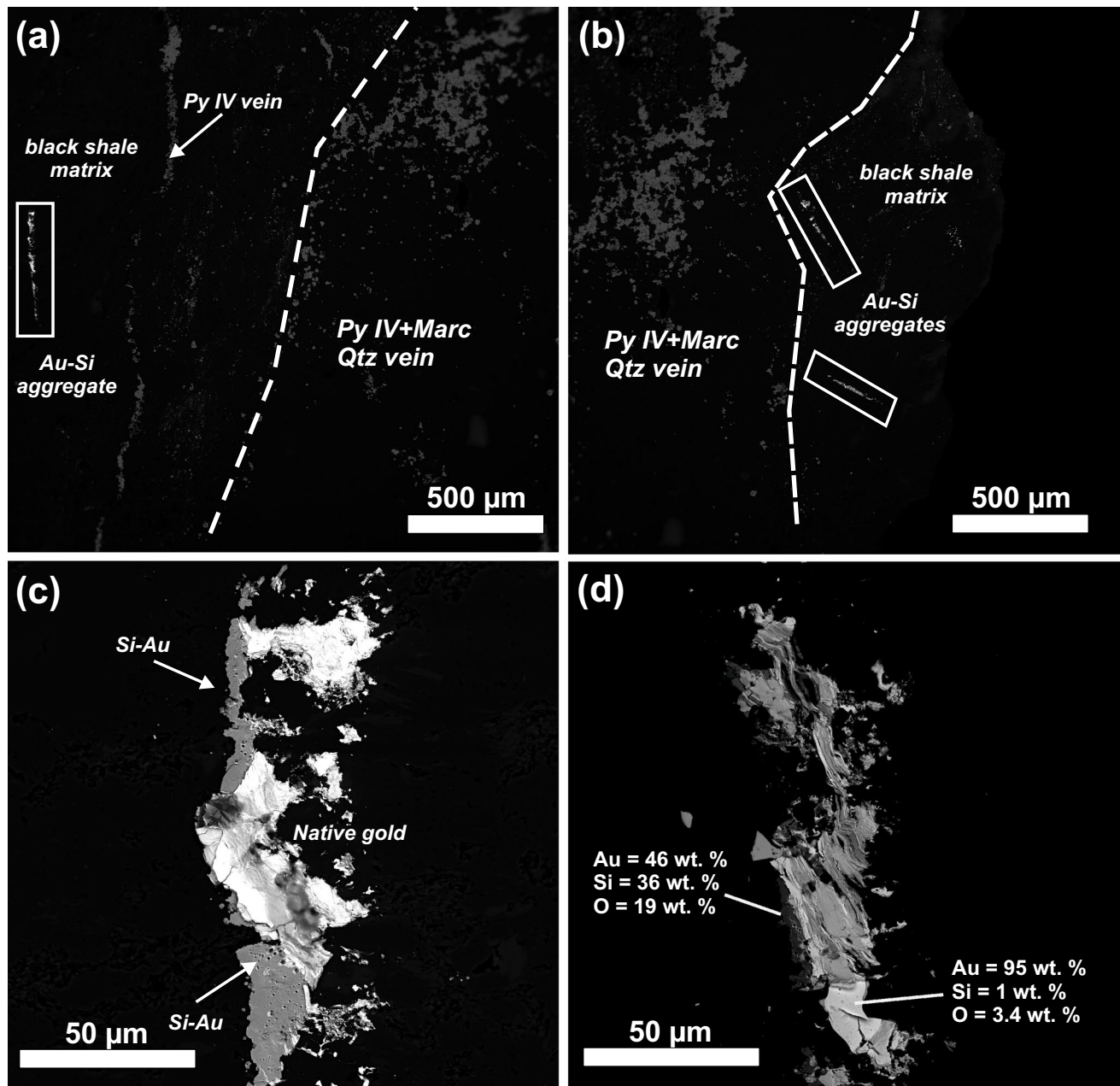
Fig. 6 Petrography of native gold and its relationship to the sulfide mineralization. **a–b** Position of Au–Si aggregates with respect to sulfide mineralization showing an intimate relationship. **c–d** Texture of native gold dendritic aggregates containing variable proportions of Si and O

although the median value for the NBS pyrite (− 14.7‰) is significantly higher than that of the SIBS pyrite (− 19.0‰).

Discussion

Depositional environment of the normal black shales

The normal black shales (NBS) exposed in the Žloukovice section exhibit largely monotonous composition

characterized by only subtle variation in major and trace element contents (Figs. 7, 8, and 9). This suggests only minor changes of the depositional environment in terms of redox conditions, supply, and nature of the siliciclastic material and also the absence of pervasive silicification. Redox conditions during deposition can be evaluated using multiple proxies such as TOC and sulfur levels or enrichment factors (EF; e.g., Algeo and Tribovillard 2009; Algeo and Liu 2020). In this respect, all lines of evidence indicate rather oxygenated or only mildly reduced conditions dominated during
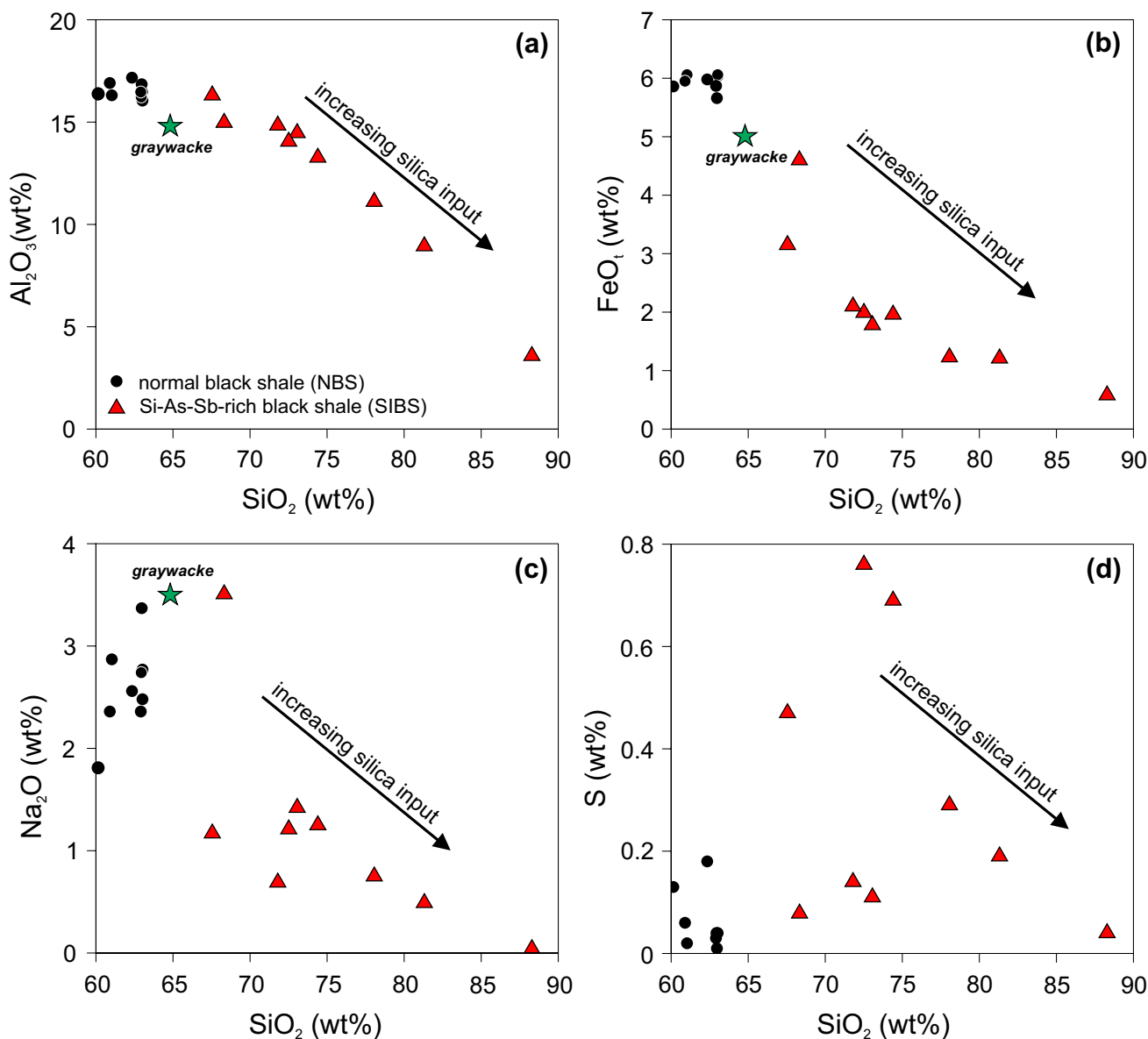
Fig. 7 a–d Variation of the selected major element oxides and sulfur in the studied black shales and local graywacke. Note an apparent increase in SiO_2 contents related to progressive infiltration of silica-rich hydrothermal fluids connected with a corresponding decrease of other major element compounds due to dilution effect

deposition of the Žloukovice black shales. Notably, the studied shales exhibit very low levels of TOC, Mo, U, V, Ni, and their EF collectively yield very low values mostly close to unity or only slightly higher (Supplementary Table 1) and TOC/P below ~ 13, well below that reported for marine phytoplankton with TOC/P of ~ 106 (Algeo and Ingall 2007).

The chondrite-normalized REE patterns of the NBS, showing mildly LREE-enriched patterns ($La_N/Yb_N = 8.1$–9.4) and marked negative Eu anomalies (Eu/Eu* of ~ 0.7), collectively point at a predominant input of these elements from a terrigenous source. The overwhelming similarity between NBS and local background represented by graywacke (Figs. 7, 8 and 9) indicates a similar source and degree of terrigenous input into the NBS-parental basin.

Lithium contents (mean [Li] = 42.5 ± 20.6 ppm) and isotopic compositions (δ^7Li from -1.7 to $+1.6‰$) in NBS samples are comparable to typical upper continental crust values (mean [Li] = 30.5 ± 3.6 ppm, mean $\delta^7Li = +0.6 \pm 0.6‰$; Teng et al. 2004; Sauzéat et al. 2015) and also lie within the range of Li elemental/isotope data obtained on black shales from the Canadian Shield (Millot et al. 2010) as well as shales from the Susquehanna Shale Hills, USA (Steinhoefel et al. 2021), indicating similar conditions of deposition. The NBS samples
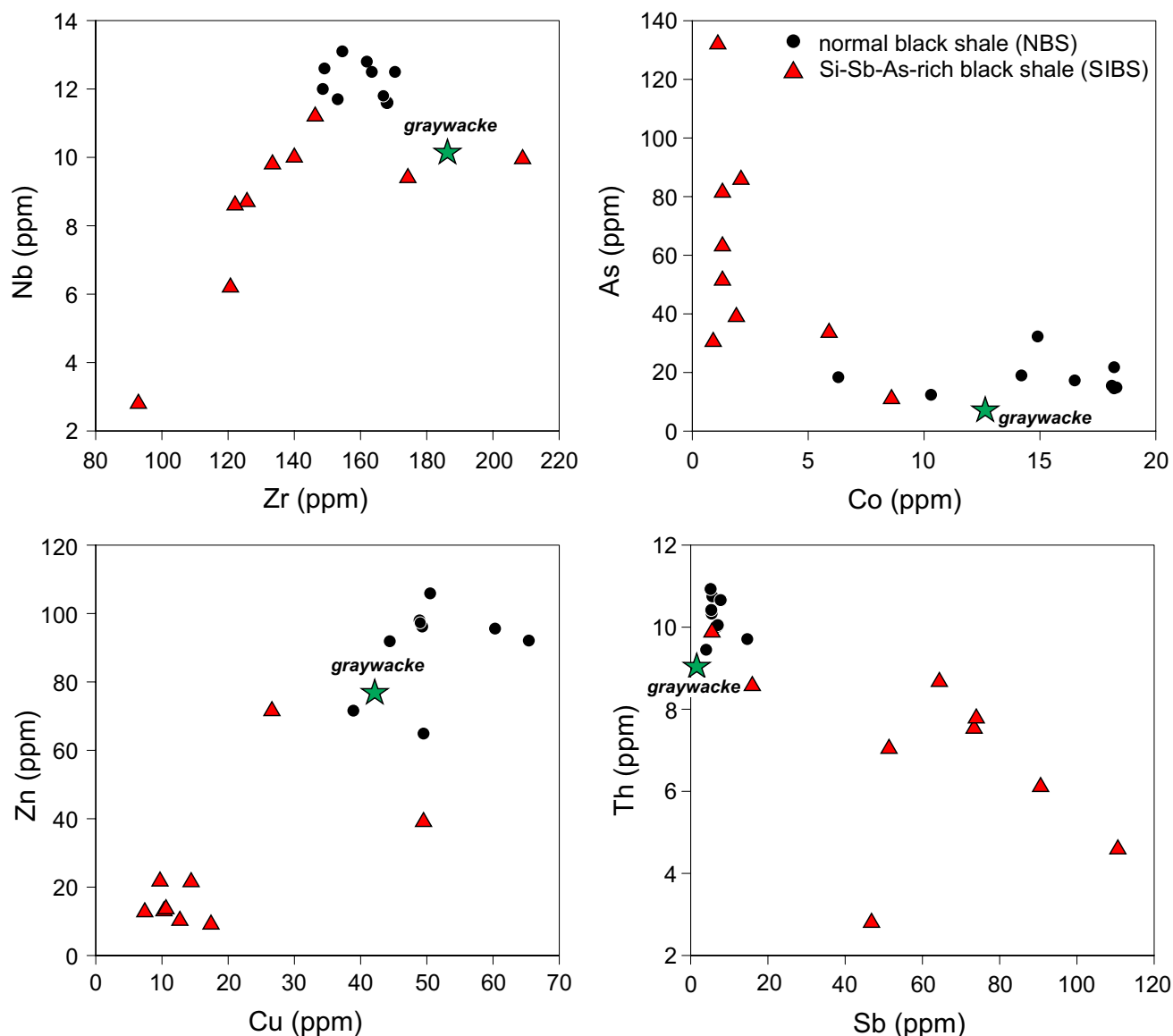
Fig. 8 **a–d** Variation of the Zr, Nb, Th, and selected metal (As, Co, Zn, Cu, Sb) contents illustrating the differences between normal (NBS) and Si–Sb–As-rich black shales

also form a coherent group indicating that they escaped any overprint by late-stage mineralizing/silica-rich fluids (Fig. 10c). The rather intact nature of these shales can also be envisaged on the basis of quartz-free matrix isolated from the NBS sample 17CB09/3 with Li isotopic composition (δ^7Li = + 0.6 ± 0.1‰) irresolvable from bulk specimen (δ^7Li = + 0.3 ± 0.2‰). The quartz-free matrix of this particular sample also displays slightly elevated δ^7Li of + 3.1‰ indicating a subordinate though non-negligible influence of such silica infiltration. This is also in agreement with field observations documenting the presence of veins in some parts of the NBS section (Fig. 2a). Collectively, the Li elemental and isotope systematics of NBS samples are fully consistent with derivation of their source

materials from the upper continental crust and lack any post-depositional modification.

The low and somewhat variable δ^{34}S values of pyrite extracted from the NBS are similar to those reported from other black shales in the Bohemian Massif (e.g., Pašava et al. 1996) and suggest formation of pyrite through variable bacterial reduction of seawater sulfate.

The interplay between deformation, mineralization and related Au enrichment

The silica-rich black shales (SIBS) at the Žloukovice section are characterized by high but variable SiO$_2$ contents causing variably low contents of other major elements, which are
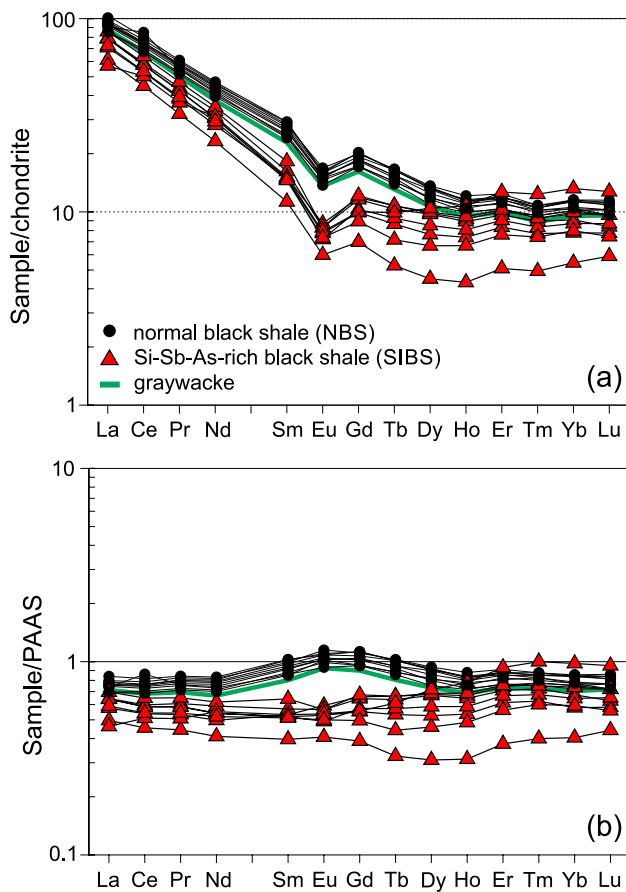
Fig. 9 Rare earth element distributions of the studied black shales and local graywacke normalized to chondrite (**a**) and post-Archean Australian Shale (**b**). The normalizing values are from Boynton (1984) and McLennan (2001), respectively

negatively correlated with SiO$_2$ due to the dilution effect (Fig. 7). This effect is also apparent in some trace elements (e.g., Co, Ni, Cu, Zn; Supplementary Table 1; Fig. 8). In contrast, SiO$_2$ contents are largely correlated with Sb concentrations (Fig. 11a) indicating an intimate relationship between input of Si and Sb. Whereas no direct relationship between SiO$_2$ and S content exists (Fig. 7d), detailed sulfide petrography and in-situ trace element analyses (Fig. 5) suggest that multiple events associated with silica addition were responsible for the overwhelming presence of several generations of sulfide phases as well as for the changes in the observed sulfide paragenesis. In parallel, detailed microstructural analyses presented above revealed that the observed SiO$_2$ enrichment can be related to three different stages of quartz vein formation (Qtz I–III) that can be closely linked to different deformation regimes and metamorphic conditions (Fig. 12). Therefore, the observed petrographic, mineralogical, structural and geochemical characteristics of the studied succession reflect a complex interplay

between primary black shale deposition and several stages of silica–sulfide enrichment as discussed in detail below.

In both the NBS and SIBS, the syndepositional to early diagenetic sulfide stage (Stage I) is represented by three different generations of pyrite (Py I–III; Fig. 4). It appears from the collected trace element data that the progressive pyrite transformation was characterized by a marked decrease in the Ni, Co, and Zn contents, paralleled by an increase in Ni/Co ratio (Table 2, Fig. 12). This is similar to the findings of Pitcairn et al. (2006) and George et al. (2018) who documented a systematic decrease in some trace element contents (e.g., Au, Ag, As, Sb) in pyrite in response to metamorphic overprint. Whereas the exact timing of Py I to II transformation is uncertain, the folded Py III layers are parallel to folded early quartz micro-veins (Qtz I) that formed during the Cadomian (late Ediacaran to early Cambrian) penetrative regional deformation and lower greenschist-facies metamorphism (Figs. 3a, 4c and 12). Therefore, these inferences provide not only an upper age limit for Py III formation, but also for the first stage of silica enrichment (Fig. 12).

The next evolutionary stage (Stage II) is associated with deformation in a brittle regime and with a large-scale infiltration of silica-rich fluids, overall expressed by the formation of undeformed late-stage quartz–sulfide veins (Qtz III) cross-cutting the black shale matrix and microfolds (Fig. 3d). Precipitated sulfides are represented by Sb-rich marcasite (up to 1.2 wt%; Table 2) and Py IV aggregates (Fig. 4e) within the quartz veins or veins of Py IV (Fig. 6a and 12). A well-developed correlation between bulk-rock SiO$_2$ and Sb contents (Fig. 11a) confirms an intimate relationship between the formation of Qtz III veins and the Sb enrichment, whereas a direct connection with As is unlikely as inferred from the lack of any correlation between SiO$_2$ and As (Fig. 9b) and from an inverse relationship between Sb and As (Fig. 9c).

The subsequent Stage III is characterized by large-scale pyritization of inner marcasite (Fig. 4f) within the Qtz III veins and, at the same time, by dissolution and resorption of Py III rims and formation of Py V (Fig. 4d). Trace element chemistry revealed that this stage was intimately associated with the input of As, Se and Au (Table 2; Fig. 5 and Fig. 12), and therefore, it documents an abrupt change in hydrothermal fluid chemistry from Sb–Hg-rich to As–Au-rich.

Native gold occurs in an intimate association with silica forming dendritic aggregates with different Si/Au ratios (~ 0.8 to 0.01) that is characteristic of colloform gold described from epithermal deposits (e.g., Saunders 2022 and references therein). This observation points to native gold having precipitated from silica- and Au-bearing low-temperature hydrothermal colloidal solutions (e.g., Pokrovski et al. 2014). Considering the positioning of Si–Au aggregates near the veins (Fig. 6c, d) and the Au-rich nature of pyritized marcasite as well as Py V (Stage III), the most
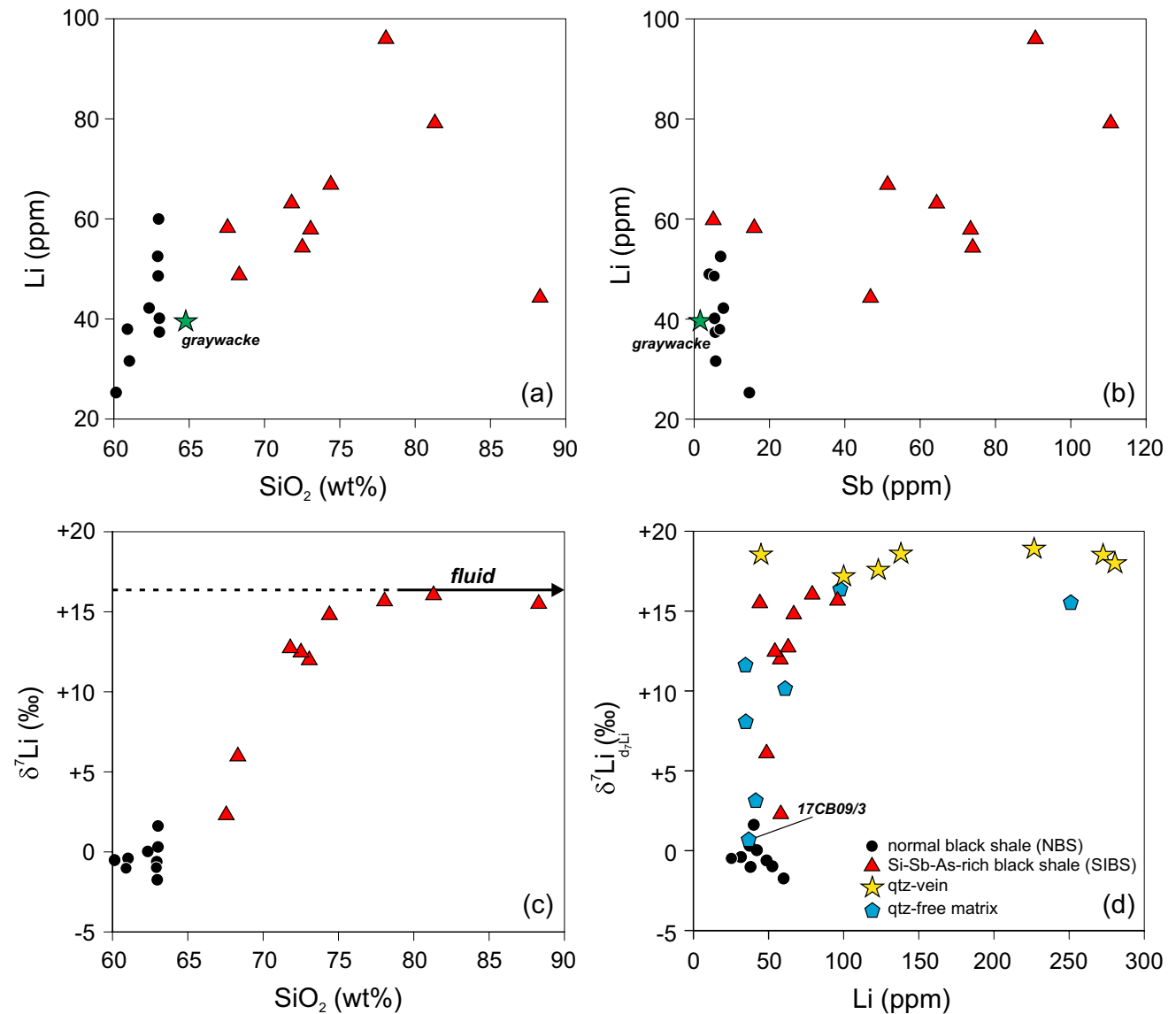
Fig. 10 a–d Lithium elemental and isotopic systematics of the studied black shales as well as quartz veins and remaining quartz-free matrix together with the relationship to variable SiO_2 and Sb contents

plausible explanation for its origin is that it represents the final, low-temperature evolutionary stage (Stage IV) of the same hydrothermal fluids parental to quartz–sulfide (Qtz III) veins.

The exact age of the Qtz III veins, and thus the associated mineralization belonging to stages III and IV, has not been determined using radiometric methods. Important temporal constraints, however, may be inferred from the field relationships and regional correlations. We have shown that the Qtz III veins cross-cutting the Cadomian cleavage (Figs. 2b and 3b, c) form a distinct, homogeneously oriented set, which is parallel to the 65°-trending axis of the southeasterly oriented Ordovician (Tremadocian) to Devonian (Givetian) Prague Basin (Figs. 1 and

2c). The vein orientation coincides with the elongation of Early to Middle Ordovician depocentres and with the trend of synsedimentary normal faults as elaborated by Havlíček (1981) and Žák et al. (2013), all indicating a common ~ NW–SE principal extension direction during opening of the basin. It has also been well established that the early-rift phase of the basin development was accompanied by extensive submarine basaltic volcanism, interpreted to had formed through mantle decompression melting in response to rifting and opening of the Rheic Ocean (Fig. 12). The reheating and subsequent cooling during rift development is also corroborated by a K–Ar illite age of 472 ± 12 Ma obtained from slate near the Žloukovice section (J. Hajná, pers. comm.). In summary, we suggest
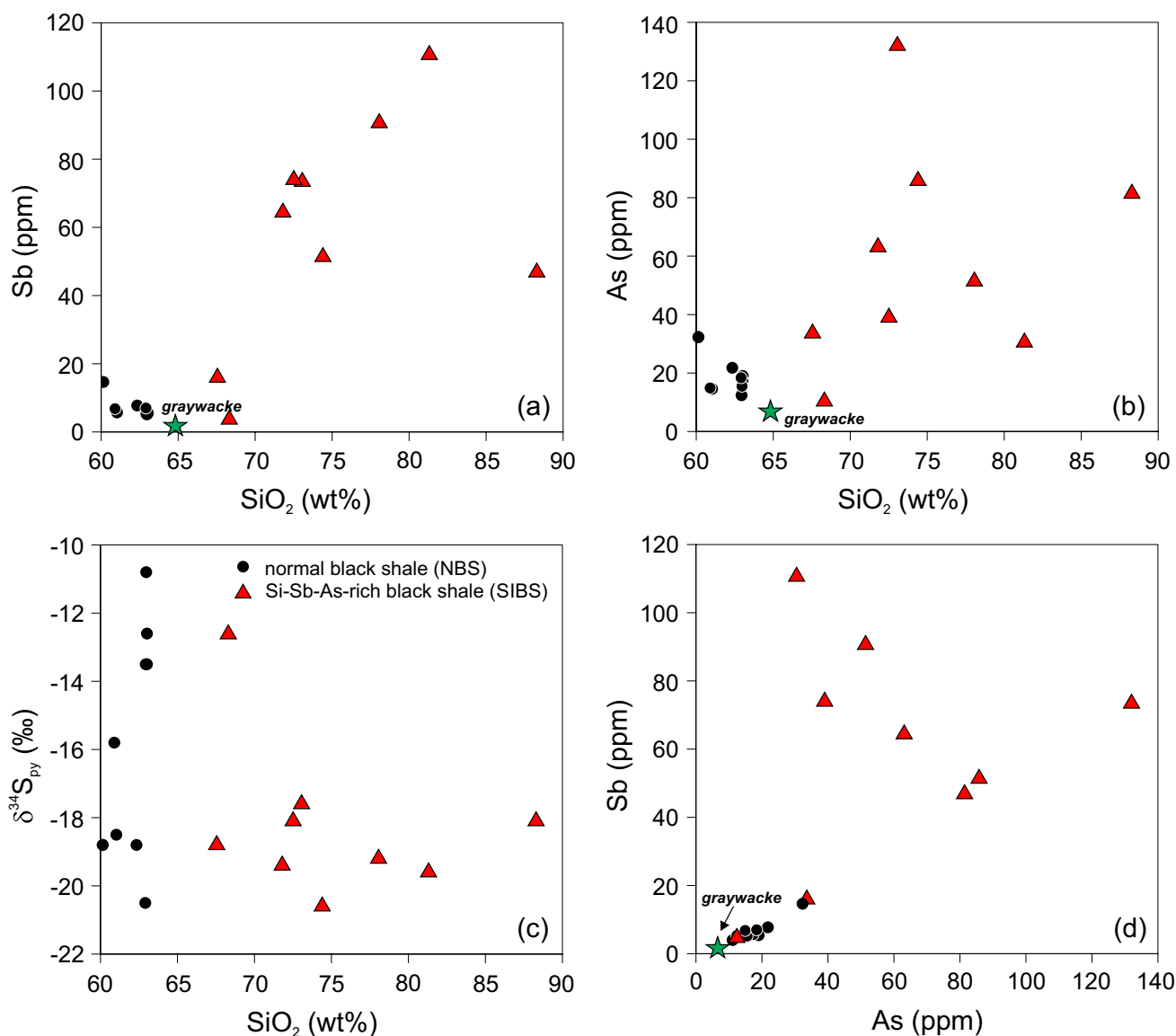
Fig. 11 **a–d** Variation of the selected metals (As, Sb) with an increasing SiO$_2$ contents and δ^{34}S values for pyrite. Note that Sb values are negatively correlated with As contents suggesting an abrupt change in the composition of mineralizing fluids from Sb-rich to As-rich (see text for more details)

that the main stages of mineralization (including Au) at Žloukovice formed in a rift setting that overprinted the previous accretionary orogenic cycle.

Nature and source of the Au-bearing hydrothermal fluids

In an attempt to constrain the possible source of the hydrothermal fluid, we consider the most silica-rich SIBS samples 17CB09/16 and 17CB09/17 as a possible end-member. The Li isotopic composition of these samples (δ^{7}Li > +15.5‰) is well above the range of other SIBS samples and given the inflection in the δ^{7}Li versus SiO$_2$ plot (Fig. 10c), we estimate the δ^{7}Li of ~ +16 ‰ to represent the pure silica-precipitating fluid component that infiltrated into the shales. Its Li abundance remains less constrained because high-δ^{7}Li samples show a range of Li contents between 44 and 96 ppm. However, the prevalent trend towards higher Li concentrations with the increasing SiO$_2$ contents is indicative of the elevated Li abundance for pure silica, estimated here at > ~ 100 ppm Li. This estimate is in accord with the elevated Li contents in quartz veins from both the NBS and SIBS sections (Table 1). The quartz veins from the NBS section are uniformly enriched in Li (> ~ 140 ppm) by a factor of ~ 4–5
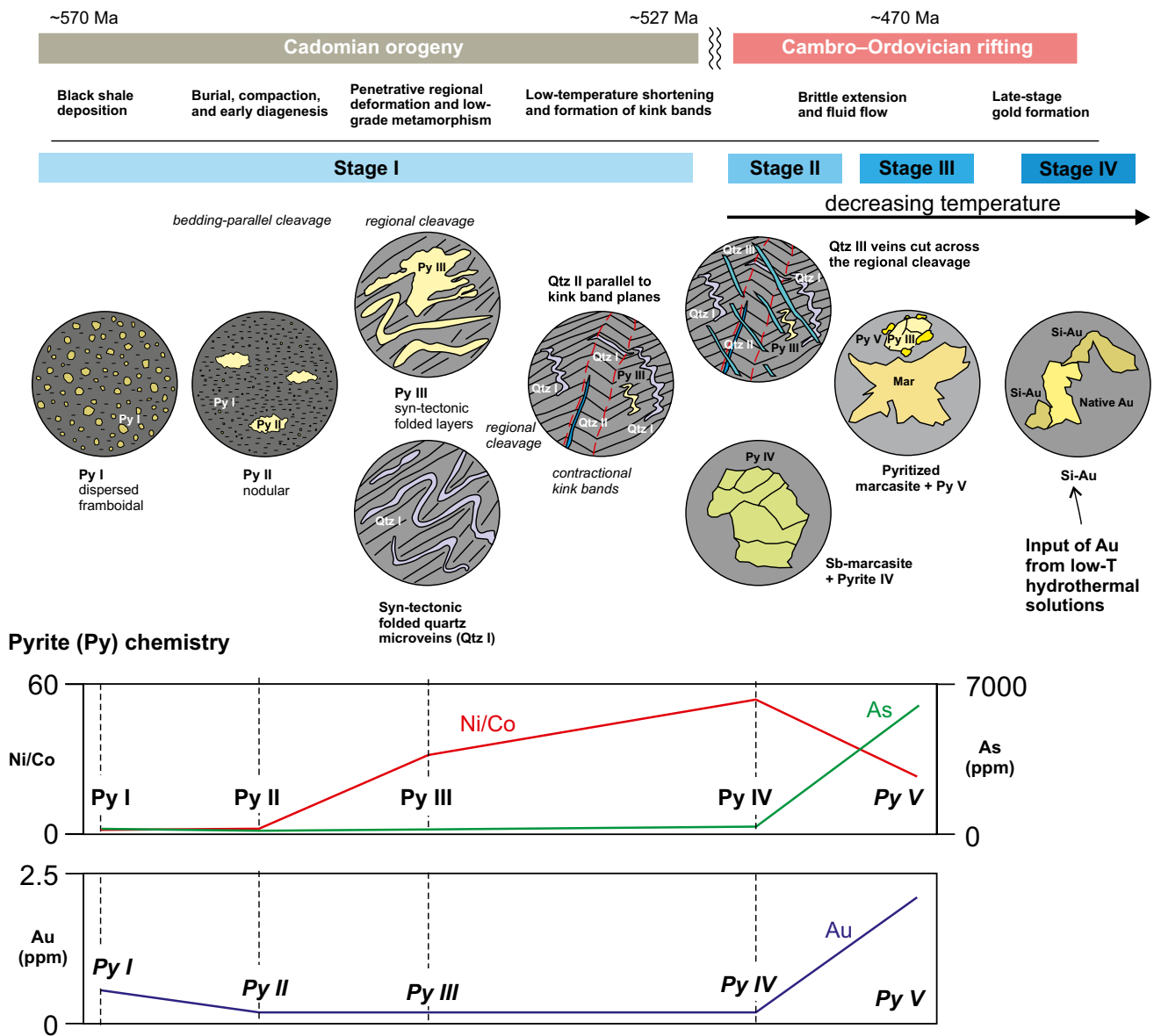
Fig. 12 Diagram showing the envisaged multi-stage evolution of silica-addition and associated mineralization in the black shales of the Žloukovice section together with changes in pyrite chemistry; see text for discussion

whereas for SIBS samples, the Li enrichment in quartz veins varies from ~1.3 to ~5 in most samples. These Li abundances are somewhat greater than those reported for quartz from the Tin Mountain pegmatite (Teng et al. 2006) and are marginally elevated compared to Li contents in fluid inclusions entrapped in quartz from the Brusson gold district, Italy (Richard et al. 2018), but are substantially greater than those in quartz from orogenic gold deposits of the Jiaodong Peninsula for which Bao et al. (2021) reported a maximum of ~10 ppm Li in quartz (but typically about 1 ppm). Similarly, low Li contents of ~1 ppm and even lower were found by Yang et al. (2015) in quartz from the Gacun volcanogenic sulfide deposit, China.

The uniformly high δ^7Li values ($\geq +17.3‰$) in NBS and SIBS quartz veins (Table 1) are consistent with the values reported by Teng et al. (2006) and Yang et al. (2015), whereas they are marginally lower than the δ^7Li of quartz given by Bao et al. (2021). Bao et al. (2021) demonstrated that Rayleigh fractionation in a closed system was responsible for the evolution of the Li isotope systematics in the Jiaodong orogenic gold deposits. In contrast, an increase in δ^7Li with decreased abundances of Au (and Cu) at La Fossa, Italy, was linked with metasomatism of pyrite and formation of α-cristobalite (Nadeau et al. 2021b). Recently, Nadeau et al. (2021a) revealed high δ^7Li of > +14‰ in Au-bearing quartz–carbonate–pyrite veinlets from the Kirkland

Lake gold deposit, Canada, which was advocated to reflect the preferential ^{7}Li incorporation in quartz as a consequence of short Li–O bond length (e.g., Magna et al. 2016), but the addition of isotopically heavy groundwater was not excluded.

Magmatic fluids derived from a rhyolitic dome and convective circulation of seawater-dominated fluids were responsible for variably elevated δ^7Li values in fluid inclusions (+4.5 to +13.8‰) and host quartz (+6.7 to +21.0‰) in the Gacun Au deposit (Yang et al. 2015). Besides, pore fluids and cold seep fluids can also have elevated δ^7Li of up to ~ +45‰ (Scholz et al. 2010). The pervasive siliceous alteration of the SIBS suite is supported by the elevated δ^7Li values (+8.0 to +16.4‰) in the black shale matrix, which are devoid of visible quartz veinlets. The calculated δ^7Li of up to +18.4‰ in the ore-forming fluids calculated by Yang et al. (2015) are within the estimate of the Li isotopic composition of late-stage silica fluids (~ +16‰) pervasively overprinting the Žloukovice SIBS succession.

We anticipate that Li could have been mobilized from the Cambrian and/or Ordovician volcanic rocks by percolating high-temperature fluids. Similar conclusions have been derived for the Cambro–Ordovician serpentinite, amphibolite, and eclogite from the Massif Central and Variscan blueschist, greenschist, eclogite, and metapelites from the Armorican Massif (both located in France), for which El Korh et al. (2020) calculated high δ^7Li of up to ~ +25‰, supposedly derived from seawater and/or hydrothermal fluids. Such fluids at hydrothermal or even hotter, super-critical conditions are known to carry preferentially ^{7}Li (e.g., Foustoukos et al. 2004; Araoka et al. 2016) and their migration could thus introduce isotopically heavy Li into the system. We also note here that whereas modern seawater has δ^7Li of ~31‰ (Misra and Froelich 2012), older seawater, including Palaeozoic, might have been significantly lower in δ^7Li (Kalderon-Asael et al. 2021) and fluids derived from such seawater could also have comparatively lower ^{7}Li/^{6}Li ratios.

Given the difficulty in isolating individual quartz vein phases for Li analysis, we are yet unable to resolve individual stages of hydrothermal input using Li elemental/isotope systematics. We note, however, that the variability in Li contents of these veins (Table 1) could provide future additional constraints on the temperature–chemistry–time–source conditions of their derivation by careful and detailed sampling.

Implications for Au metallogeny in the Bohemian Massif and other Cadomian-basement domains

Overall, the chemistry of pyrite formed through the protracted evolution (*stages I* to *III*), combined with the presence of Sb-rich marcasite, points to a predominantly external source of indicative metals (e.g., Sb, As, Au), but remobilization from the Py I–III generations hosted by local NBS

cannot be completely ruled out (these are Sb–As–Au-poorer; Table 2). As discussed above, the formation of quartz veinlets is most likely related to Ordovician (~ 470 Ma) rifting and volcanism, and therefore, the detected Sb–As–Au mineralization represents a product of related hydrothermal fluid circulation leading to metal remobilization from either the surrounding volcano-sedimentary successions or Ordovician volcanic rocks themselves. The former would agree with the spatial connection between the Variscan gold deposits/occurrences in the Bohemian Massif and Neoproterozoic–Cambrian volcano-sedimentary successions indicative of the sourcing of metals including Au from these formations (Morávek and Pouba 1987). Similarly, the rather uniform δ^{34}S values of pyrite detected in the studied black shales (–18.9 ± 1.0 ‰; Table 1) suggest sulfur remobilization from some reduced sedimentary rocks such as black shales. Finally, we document that Py I → Py III transformation related to late Ediacaran to early Cambrian deformation and metamorphism was also connected with significant release of some metals, including Au (Table 2).

Apparently, the Au mineralization documented in this study is genetically different from the Variscan-type Au deposits found elsewhere in the Bohemian Massif (see Romer and Kroner 2018 for an overview) where gold typically forms either micron-sized inclusions within sulfides (e.g., Mokrsko and Jílové deposits; Zachariáš et al. 2013; Zachariáš et al. 2014) or has been found in quartz–stibnite (As–Sb) veins (e.g., Krásná Hora; Němec and Zachariáš 2017). Furthermore, it is also different from the volcanogenic-massive sulfide mineralization of the Besshi-type that is considered to be related to Cambro–Ordovician magmatic activity (e.g., Tisová in the Saxothuringian Zone, northeastern Bohemian Massif; Dill 1989; Pertold et al. 1994) or Au occurrences within Ordovician sandstones also in the Saxothuringian Zone (Romer and Kroner 2018).

Although our new report on shale-hosted gold is based on only a single locality with no economic importance, its elemental association (Sb–As–Au) and the suggested linkage to the Cambro–Ordovician rifting and associated magmatism is potentially interesting for future gold exploration for several reasons. First, in spite of several attempts to prospect for gold in the Neoproterozoic–Cambrian black shales undertaken during the 1980s and 1990s, which occasionally revealed elevated Au contents (Pouba and Kříbek 1986; Morávek and Pouba 1987; Pašava et al. 1996), the nature and source for the Au enrichment have not been deciphered so far. Our study documents that Au mineralization may not be directly related only to black shale matrix, but to late-stage quartz veinlets penetrating these shale successions similarly as some significant quartz vein-hosted gold deposits from the Caledonian orogenic belt of northern Great Britain (Rice et al. 2016). Second, the inferred genetic link with Ordovician magmatic activity is in contradiction to the previously

assumed Ordovician sedimentary source for Au (sandstone-hosted gold placers; Romer and Kroner 2018) and rather indicates that magmatic heating can serve as an efficient trigger for metal and sulfur remobilization from the Proterozoic–Cambrian volcano-sedimentary precursors. Finally, while the Cambrian–Ordovician magmatic stage represents a widespread event in the Bohemian Massif, notably in the Teplá–Barrandian Unit, the connection with possible Au mineralization has not been established so far. Thus, we highlight that this magmatic stage might play an important role not only in the metallogeny of the Bohemian Massif but also in other Cadomian-basement domains with similar evolution and metallogeny (e.g., Iberian and Armorican Massifs in Spain and France, respectively) and should thus be considered potential targets in future exploration efforts.

Conclusions

(1) A new occurrence of Au mineralization in Late Neoproterozoic (Ediacaran) black shales was discovered in the Bohemian Massif. The black shales were deposited in deep sea at an active plate margin under predominantly oxygenated conditions and supplied by both organic matter and fine-grained terrigenous material from a nearby volcanic arc.

(2) The Au enrichment is related to the formation of a quartz–sulfide vein system within the black shales and is a result of a progressive evolution of ore-forming fluids with decreasing temperatures from Sb-rich to As-rich to precipitation of native gold from Au-bearing low-temperature hydrothermal solutions.

(3) The structural relationships and orientation of quartz veins associated with the Au mineralization suggest an intimate connection between the vein emplacement and Ordovician high heat flow in response to rifting and breakup of the northern margin of Gondwana and opening of the Rheic Ocean.

(4) Lithium contents and isotope data largely preclude the black shales as a source and, instead, they indicate derivation of Li from late-stage hydrothermal fluids and/or seawater.

(5) Ordovician heating due to crustal thinning likely served as a trigger for metal and sulfur remobilization including Au from the associated Neoproterozoic–Cambrian volcano-sedimentary successions. Yet, in our case, local black shale successions are unlikely to had served as a major source of Au, S, and other related metals; however, a partial Au remobilization cannot be completely ruled out.

(6) The newly documented type of Au mineralization and its association with the Ordovician rift-related magmatic activity is different from the prevalent, Variscan-type of gold occurrences reported so far in the Bohemian Massif. Therefore, our study provides a new genetic interpretation potentially important for future exploration of Au not only in the Bohemian Massif but also in other basement terrains that host black shale successions and underwent post-depositional heating, hydrothermal flow, and remobilization of Au due to lithospheric extension and rifting.

Declarations

Conflict of interest The authors declare no competing interests.

References

Ackerman L, Žák K, Haluzová E, Creaser RA, Svojtka M, Pašava J, Veselovský F (2019) Chronology of the Kašperské Hory orogenic gold deposit, Bohemian Massif, Czech Republic. Miner Depos 54:473–484

Ackerman L, Žák J, Kachlík V, Pašava J, Žák K, Pack A, Veselovský F, Strnad L (2023) The significance of cherts as markers of

Ocean Plate Stratigraphy and paleoenvironmental conditions: new insights from the Neoproterozoic–Cambrian Blovice accretionary wedge. Bohemian Massif Geosci Front 14:101478

Aichler J, Fojt B, Cháb J, Kvaček M, Novotný P, Orel P, Vaněček M (1990) Gold-bearing mineralization at the locality Suchá Rudná in the Jeseníky Mts. Sb Geol Věd Ložisk Geol Mineral 29:79–107

Algeo TJ, Ingall E (2007) Sedimentary Corg: P ratios, paleocean ventilation, and Phanerozoic atmospheric p_O2. Palaeogeogr Palaeoclimatol Palaeoecol 256:130–155

Algeo TJ, Liu J (2020) A re-assessment of elemental proxies for paleoredox analysis. Chem Geol 540:119549

Algeo TJ, Tribovillard N (2009) Environmental analysis of paleoceanographic systems based on molybdenum–uranium covariation. Chem Geol 268:211–225

Araoka D, Nishio Y, Gamo T, Yamaoka K, Kawahata H (2016) Lithium isotopic systematics of submarine vent fluids from arc and back-arc hydrothermal systems in the western Pacific. Geochem Geophys Geosyst 17:3835–3853

Bao C, Chen B, Liu C, Zheng J, Liu S (2021) Lithium isotopic systematics of ore-forming fluid in the orogenic gold deposits, Jiaodong Peninsula (East China): implications for ore-forming mechanism. Ore Geol Rev 136:104254

Belousov I, Large RR, Meffre S, Danyushevsky LV, Steadman J, Beardsmore T (2016) Pyrite compositions from VHMS and orogenic Au deposits in the Yilgarn Craton, Western Australia: implications for gold and copper exploration. Ore Geol Rev 79:474–499

Böning P, Fröllje H, Beck M, Schnetger B, Brumsack HJ (2012) Underestimation of the authigenic fraction of Cu and Ni in organic-rich sediments. Mar Geol 323–325:24–28

Boynton WV (1984) Cosmochemistry of the rare earth elements: meteorite studies. In: Henderson P (ed) Rare earth element geochemistry. Elsevier, Amsterdam, pp 63–114

Brumsack HJ (2006) The trace metal content of recent organic carbon-rich sediments: implications for Cretaceous black shale formation. Palaeogeogr Palaeoclimatol Palaeoecol 232:344–361

Chlupáč I, Havlíček V, Kříž J, Kukal Z, Štorch P (1998) Palaeozoic of the Barrandian. Czech Geological Survey, Prague

Coveney RM, Pašava J (2004) Diverse connections between ores and organic matter. Ore Geol Rev 24:1–5

Deditius AP, Reich M, Kesler SE, Utsunomiya S, Chryssoulis SL, Walshe J, Ewing RC (2014) The coupled geochemistry of Au and As in pyrite from hydrothermal ore deposits. Geochim Cosmochim Acta 140:644–670

Dempírová L, Šikl J, Kašičková R, Zoulková V, Kříbek B (2010) The evaluation of precision and relative error of the main components of silicate analyses in Central Laboratory of the Czech Geological Survey. Geosci Res Rep 27:326–330

Dill HG (1989) Metallogenetic and geodynamic evolution in the central European Variscides - a pre-well site study for the German continental deep drilling programme. Ore Geol Rev 4:279–304

Drost K, Linnemann U, McNaughton N, Fatka O, Kraft P, Gehmlich M, Tonk C, Marek J (2004) New data on the Neoproterozoic-Cambrian geotectonic setting of the Teplá-Barrandian volcano-sedimentary successions: geochemistry, U-Pb zircon ages, and provenance (Bohemian Massif, Czech Republic). Int J Earth Sci 93:742–757

Drost K, Gerdes A, Jeffries T, Linnemann U, Storey C (2011) Provenance of Neoproterozoic and early Paleozoic siliciclastic rocks of the Teplá-Barrandian unit (Bohemian Massif): Evidence from U-Pb detrital zircon ages. Gondwana Res 19:213–231

Edel JB, Schulmann K, Lexa O, Lardeaux JM (2018) Late Palaeozoic palaeomagnetic and tectonic constraints for amalgamation of Pangea supercontinent in the European Variscan belt. Earth-Science Rev 177:589–612

El Korh A, Deloule E, Luais B, Boiron M-C, Bastian L, Vigier N (2020) Lithium behaviour and isotope fractionation during fluid–rock interactions in Variscan oceanic suture zones: Limousin ophiolite and Ile de Groix high-pressure terrane (France). J Petrol 60:1963–1990

Flesch GD, Anderson AR, Svec HJ (1973) A secondary isotopic standard for $^6Li/^7Li$ determinations. Int J Mass Spectrom Ion Phys 12:265–272

Foustoukos DI, James RH, Berndt ME, Seyfried WE Jr (2004) Lithium isotopic systematics of hydrothermal vent fluids at the Main Endeavour Field, Northern Juan de Fuca Ridge. Chem Geol 212:17–26

Franke W (2006) The Variscan orogen in Central Europe: construction and collapse. Geol Soc Mem 32:333–343

George LL, Biagioni C, D'Orazio M, Cook NJ (2018) Textural and trace element evolution of pyrite during greenschist facies metamorphic recrystallization in the southern Apuan Alps (Tuscany, Italy): influence on the formation of Tl-rich sulfosalt melt. Ore Geol Rev 102:59–105

Hajná J, Žák J, Kachlík V, Chadima M (2010) Subduction-driven shortening and differential exhumation in a Cadomian accretionary wedge: the Teplá-Barrandian unit, Bohemian Massif. Precambrian Res 176:27–45

Hajná J, Žák J, Kachlík V, Dörr W, Gerdes A (2013) Neoproterozoic to early Cambrian Franciscan-type mélanges in the Teplá-Barrandian unit, Bohemian Massif: evidence of modern-style accretionary processes along the Cadomian active margin of Gondwana? Precambrian Res 224:653–670

Hajná J, Žák J, Dörr W, Kachlík V, Sláma J (2018) New constraints from detrital zircon ages on prolonged, multiphase transition from the Cadomian accretionary orogen to a passive margin of Gondwana. Precambrian Res 317:159–178

Hajná J, Žák J, Ackerman L, Svojtka M, Pašava J (2019) A giant late Precambrian chert-bearing olistostrome discovered in the Bohemian Massif: a record of Oceanic Plate Stratigraphy (OPS) disrupted by mass-wasting along an outer trench slope. Gondwana Res 74:173–188

Havlíček P (1981) Development of a linear sedimentary depression exemplified by the Prague Basin (Ordovician–Middle Devonian; Barrandian area—central Bohemia). Sborník Geol Věd Řada Geol 35:7–48

Hu S-Y, Evans K, Fisher L, Rempel K, Craw D, Evans NJ, Cumberland S, Robert A, Grice K (2016) Associations between sulfides, carbonaceous material, gold and other trace elements in polyframboids: implications for the source of orogenic gold deposits, Otago Schist, New Zealand. Geochim Cosmochim Acta 180:197–213

Jochum KP, Nohl U, Herwig K, Lammel E, Stoll B, Hofmann AW (2005) GeoReM: a new geochemical database for reference materials and isotopic standards. Geostand Geoanalytical Res 29:333–338

Kalderon-Asael B, Katchinoff JAR, Planavsky NJ, Hood AS, Dellinger M, Bellefroid EJ, Jones DS, Hofmann A, Ossa FO, Macdonald FA, Asael D, Pogge von Strandmann PAE (2021) A lithium-isotope perspective on the evolution of carbon and silicon cycles. Nature 595:394–398

Kolářová K, Černý J, Melichar R, Schnabl P, Gaidzik K (2022) Reconstruction of ancient volcanic complexes using magnetic signature: a case study from Cambrian andesite lava flow. Bohemian Massif J Volcanol Geotherm Res 428:107591

Kroner U, Romer RL (2013) Two plates - many subduction zones: the Variscan orogeny reconsidered. Gondwana Res 24:298–329

Kurzweil F, Drost K, Pašava J, Wille M, Taubald H, Schoeckle D, Schoenberg R (2015) Coupled sulfur, iron and molybdenum isotope data from black shales of the Teplá-Barrandian unit

argue against deep ocean oxygenation during the Ediacaran. Geochim Cosmochim Acta 171:121–142

Large RR, Danyushevsky L, Hollit C, Maslennikov V, Meffre S, Gilbert S, Bull S, Scott R, Emsbo P, Thomas H, Singh B, Foster J (2009) Gold and trace element zonation in pyrite using a laser imaging technique: implications for the timing of gold in orogenic and carlin-style sediment-hosted deposits. Econ Geol 104:635–668

Large RR, Bull SW, Maslennikov VV (2011) A carbonaceous sedimentary source-rock model for Carlin-type and orogenic gold deposits. Econ Geol 106:331–358

Large RR, Gregory DD, Steadman JA, Tomkins AG, Lounejeva E, Danyushevsky LV, Halpin JA, Maslennikov V, Sack PJ, Mukherjee I, Berry R, Hickman A (2015) Gold in the oceans through time. Earth Planet Sci Lett 428:139–150

Lehmann B, Frei R, Xu L, Mao J (2016) Early Cambrian black shale-hosted Mo-Ni and V mineralization on the rifted margin of the Yangtze platform, China: Reconnaissance chromium isotope data and a refined metallogenic model. Econ Geol 111:89–103

Linnemann U, McNaughton NJ, Romer RL, Gehmlich M, Drost K, Tonk C (2004) West African provenance for Saxo-Thuringia (Bohemian Massif): did Armorica ever leave pre-Pangean Gondwana? U/Pb-SHRIMP zircon evidence and the Nd-isotopic record. Int J Earth Sci 93:683–705

Little SH, Vance D, Lyons TW, McManus J (2015) Controls on trace metal authigenic enrichment in reducing sediments: insights from modern oxygen-deficient settings. Am J Sci 315:77–119

Loukola-Ruskeeniemi K, Heino T (1996) Geochemistry and genesis of the black shale-hosted Ni–Cu–Zn deposit at Talvivaara, Finland. Econ Geol 91:80–110

Magna T, Wiechert UH, Halliday AN (2004) Low-blank isotope ratio measurement of small samples of lithium using multiple-collector ICPMS. Int J Mass Spectrom 239:67–76

Magna T, Wiechert U, Halliday AN (2006) New constraints on the lithium isotope compositions of the Moon and terrestrial planets. Earth Planet Sci Lett 243:336–353

Magna T, Novák M, Cempírek J, Janoušek V, Ullmann CV, Wiechert U (2016) Crystallographic control on lithium isotope fractionation in Archean to Cenozoic lithium–cesium–tantalum pegmatites. Geology 44:655–658

McLennan SM (2001) Relationships between the trace element composition of sedimentary rocks and upper continental crust. Geochem Geophys Geosyst 2:2000GC000109

Mehrabi B, Yardley BWD (1999) Sediment-Hosted Disseminated Gold Mineralisation. Miner Depos 34:673–696

Millot R, Vigier N, Gaillardet J (2010) Behaviour of lithium and its isotopes during weathering in the Mackenzie Basin, Canada. Geochim Cosmochim Acta 74:3897–3912

Misra S, Froelich PN (2012) Lithium isotope history of cenozoic seawater: changes in silicate weathering and reverse weathering. Science 335:818–823

Morávek P (1996) Gold deposits in Bohemia. Czech Geological Survey, Praha

Morávek P, Pouba Z (1987) Precambrian and Phanerozoic history of gold mineralization in the Bohemian Massif. Econ Geol 82:2098–2114

Nadeau O, Voinot A, Leybourne M (2021a) Lithium isotopes at gold deposits: insights from the giant Kirkland Lake Gold Deposit. Canada Precambrian Res 362:106308

Nadeau O, Mick E, Robidoux P, Grassa F, Brusca L, Voinot A, Leybourne MI (2021b) Lithium isotopes and Cu–Au concentrations in hydrothermal alterations from Solfatara Volcano, Campi Flegrei caldera complex, and La Fossa volcano, Vulcano Island, Italy: insights into epithermal ore forming environments. Ore Geol Rev 130:103934

Nance RD, Gutiérrez-Alonso G, Keppie JD, Linnemann U, Murphy JB, Quesada C, Strachan RA, Woodcock NH (2010) Evolution of the Rheic Ocean. Gondwana Res 17:194–222

Němec M, Zachariáš J (2017) The Krásná Hora, Milešov and Příčovy Sb–Au ore deposits, Bohemian Massif: mineralogy, fluid inclusions and stable isotope constraints on the deposit formation. Miner Depos 53:225–244

Oszczepalski S (1989) Kupferschiefer in southwestern Poland: sedimentary environments, metal zoning, and ore controls. Geol Assoc Canada Spec Pap 36:571–600

Pašava J (2000) Normal versus metal-rich black shales in the Barrandian Neoproterozoic of the Teplá-Barrandian Unit: a summary with new data. Bull Czech Geol Surv 75:229–240

Pašava J, Hladíková J, Dobeš P (1996) Origin of Proterozoic black shales from the Bohemian Massif, Czech Republic. Econ Geol 91:63–79

Pašava J, Frimmel H, Vymazalová A, Dobes P, Jukov AV, Koneev RI (2013) A two-stage evolution model for the Amantaytau orogenic-type gold deposit in Uzbekistan. Miner Depos 48:825–840

Pašava J, Ackerman L, Halodová P, Pour O, Ďurišová J, Zaccarini F, Aiglsperger T, Vymazalová A (2017) Concentrations of platinum-group elements (PGE), Re and Au in arsenian pyrite and millerite from Mo–Ni–PGE–Au black shales (Zunyi region, Guizhou Province, China): Results from LA-ICPMS study. Eur J Mineral 29:623–633

Pašava J, Ackerman L, Žák J, Veselovský F, Creaser RA, Svojtka M, Luais B, Pour O, Šebek O, Trubač J, Vosáhlová E, Cividini D (2021) Elemental and isotopic compositions of trench-slope black shales, Bohemian Massif, with implications for oceanic and atmospheric oxygenation in early Cambrian. Palaeogeogr Palaeoclimatol Palaeoecol 564:110195

Pašava J, Veselovský F, Pour O, Magna T, Dobeš P, Ackerman L, Svojtka M, Žák J, Hajná J (2018) Gold mineralization in Ediacaran black shales from the Bohemian Massif (Czech Republic). IMA 2018 Meet Proc

Patočka F, Vlašímský P, Blechová K (1993) Geochemistry of Early Paleozoic volcanics of the Barrandian Basin (Bohemian Massif, Czech Republic): Implications for Paleotectonic Reconstructions. Jahrb Geol Bundesanstalt 136:873–896

Pertold Z, Chrt J, Budil V, Burda J, Burdová P, Kříbek B, Pertoldová J, Gaskarth B (1994) The Tisová Cu-deposit: a Besshi-type mineralization in the Krušné hory Mts. Bohemian Massif Miner Depos Monogr Ser 31:71–95

Pitcairn IK, Teagle DAH, Craw D, Olivo GR, Kerrich R, Brewer TS (2006) Sources of metals and fluids in orogenic gold deposits: insights from the Otago and Alpine schists, New Zealand. Econ Geol 101:1525–1546

Pokrovski GS, Akinfiev NN, Borisova AY, Zotov AV, Kouzmanov K (2014) Gold speciation and transport in geological fluids: insights from experiments and physical-chemical modelling. Geol Soc Spec Publ 402:9–70

Pouba Z, Kříbek B (1986) Organic matter and the concentration of metals in Precambrian stratiform deposits of the Bohemian Massif. Precambrian Res 33:225–237

Reich M, Kesler SE, Utsunomiya S, Palenik CS, Chryssoulis SL, Ewing RC (2005) Solubility of gold in arsenian pyrite. Geochim Cosmochim Acta 69:2781–2796

Rice CM, Mark DF, Selby D, Neilson JE, Davidheiser-Kroll B (2016) Age and geologic setting of quartz vein-hosted gold mineralization at Curraghinalt, Northern Ireland: implications for genesis and classification. Econ Geol 111:127–150

Richard A, Banks DA, Hendriksson N, Lahaye Y (2018) Lithium isotopes in fluid inclusions as tracers of crustal fluids: an exploratory study. J Geochemical Explor 184:158–166

Romer RL, Cuney M (2018) Phanerozoic uranium mineralization in Variscan Europe – more than 400 Ma of tectonic, supergene,

and climate-controlled uranium redistribution. Ore Geol Rev 102:474–504

Romer RL, Kroner U (2018) Paleozoic gold in the Appalachians and Variscides. Ore Geol Rev 92:475–505

Sack PJ, Large RR, Gregory DD (2018) Geochemistry of shale and sedimentary pyrite as a proxy for gold fertility in the Selwyn basin area, Yukon. Miner Depos 53:997–1018

Saunders JA (2022) Colloids and nanoparticles: implications for hydrothermal precious metal ore formation. SEG Discov 15–21

Sauzéat L, Rudnick RL, Chauvel C, Garçon M, Tang M (2015) New perspectives on the Li isotopic composition of the upper continental crust and its weathering signature. Earth Planet Sci Lett 428:181–192

Scholz F, Hensen C, De Lange GJ, Haeckel M, Liebetrau V, Meixner A, Reitz A, Romer RL (2010) Lithium isotope geochemistry of marine pore waters - insights from cold seep fluids. Geochim Cosmochim Acta 74:3459–3475

Schulmann K, Edel JB, Martínez Catalán JR, Mazur S, Guy A, Lardeaux JM, Ayarza P, Palomeras I (2022) Tectonic evolution and global crustal architecture of the European Variscan belt constrained by geophysical data. Earth Sci Rev 234:104195

Selvaraja V, Fiorentini ML, Jeon H, Savard DD, LaFlamme CK, Guagliardo P, Caruso S, Bui T-H (2017) Evidence of local sourcing of sulfur and gold in an Archaean sediment-hosted gold deposit. Ore Geol Rev 89:909–930

Sláma J, Dunkley DJ, Kachlík V, Kusiak MA (2008) Transition from island-arc to passive setting on the continental margin of Gondwana: U-Pb zircon dating of Neoproterozoic metaconglomerates from the SE margin of the Teplá-Barrandian Unit, Bohemian Massif. Tectonophysics 461:44–59

Steadman JA, Large RR, Meffre S, Olin PH, Danyushevsky LV, Gregory DD, Belousov I, Lounejeva E, Ireland TR, Holden P (2015) Synsedimentary to early diagenetic gold in Black shale-hosted pyrite nodules at the Golden Mile deposit, Kalgoorlie, Western Australia. Econ Geol 110:1157–1191

Steinhoefel G, Brantley SL, Fantle MS (2021) Lithium isotopic fractionation during weathering and erosion of shale. Geochim Cosmochim Acta 295:155–177

Strnad L, Mihaljevič M, Šebek O (2005) Laser ablation and solution ICP-MS determination of rare earth elements in USGS BIR-1G, BHVO-2G and BCR-2G glass reference materials. Geostand Geoanalytical Res 29:303–314

Teng FZ, McDonough WF, Rudnick RL, Dalpé C, Tomascak PB, Chappell BW, Gao S (2004) Lithium isotopic composition and concentration of the upper continental crust. Geochim Cosmochim Acta 68:4167–4178

Teng FZ, Mcdonough WF, Rudnick RL, Walker RJ, Sirbescu M-LC (2006) Lithium isotopic systematics of granites and pegmatites from the Black Hills, South Dakota. Am Mineral 91:1488–1498

Timmermann H, Štědrá V, Gerdes A, Noble SR, Parrish RR, Dörr W (2004) The problem of dating high-pressure metamorphism: a U-Pb isotope and geochemical study on eclogites and related rocks of the Mariánské Lázně Complex, Czech Republic. J Petrol 45:1311–1338

Tomascak PB, Magna T, Dohmen R (2016) Advances in lithium isotope geochemistry. Springer International Publishing, Cham, Switzerland

Tribovillard N, Algeo TJ, Baudin F, Riboulleau A (2012) Analysis of marine environmental conditions based on molybdenum–uranium covariation-Applications to Mesozoic paleoceanography. Chem Geol 324–325:46–58

van Achterbergh E, Ryan CG, Jackson SE, Griffin WL (2001) Data reduction software for LA-ICP-MS. In: Sylvester PJ (ed) Laser-ablation-ICPMS in the Earth sciences: principles and applications. Mineralogical Association of Canada, pp 239–243

Wang J, Liu J, Peng R, Liu Z, Zhao B, Li Z, Wang Y, Liu C (2014) Gold mineralization in Proterozoic black shales: example from the Haoyaoerhudong gold deposit, northern margin of the North China Craton. Ore Geol Rev 63:150–159

Yang D, Hou Z, Zhao Y, Hou K, Yang Z, Tian S, Fu Q (2015) Lithium isotope traces magmatic fluid in a seafloor hydrothermal system. Sci Rep 5:13812

Zachariáš J, Pertold Z, Pudilová M, Žák K, Pertoldová J, Stein H, Markey R (2001) Geology and genesis of Variscan porphyry-style gold mineralization, Petráčkova hora deposit, Bohemian Massif, Czech Republic. Miner Depos 36:517–541

Zachariáš J, Žák K, Pudilová M, Snee LW (2013) Multiple fluid sources/pathways and severe thermal gradients during formation of the Jílové orogenic gold deposit, Bohemian Massif, Czech Republic. Ore Geol Rev 54:81–109

Zachariáš J, Morávek P, Gadas P, Pertoldová J (2014) The Mokrsko-West gold deposit, Bohemian Massif, Czech Republic: mineralogy, deposit setting and classification. Ore Geol Rev 58:238–263

Žák J, Kraft P, Hajná J (2013) Timing, styles, and kinematics of Cambro-Ordovician extension in the Teplá–Barrandian Unit, Bohemian Massif, and its bearing on the opening of the Rheic Ocean. Int J Earth Sci 102:415–433

Žák J, Svojtka M, Hajná J, Ackerman L (2020) Detrital zircon geochronology and processes in accretionary wedges. Earth Sci Rev 207:103214